

On the Upstream Track Deflection of Tropical Cyclones Past a Mountain Range: Idealized Experiments

CHING-YUANG HUANG AND CHIEN-AN CHEN

Department of Atmospheric Sciences, National Central University, Jhongli, Taiwan

SHU-HUA CHEN

Department of Land, Air and Water Resources, University of California, Davis, Davis, California

DAVID S. NOLAN

Rosenstiel School of Marine and Atmospheric Science, University of Miami, Miami, Florida

(Manuscript received 4 August 2015, in final form 10 May 2016)

ABSTRACT

Upstream track deflection of a propagating cyclonic vortex past an isolated mountain range is investigated by using idealized simulations with both boundary layer turbulent mixing and cloud effects. The westbound vortex past a shorter mountain range may experience an earlier northward deflection prior to landfall. The vortex then takes a sudden southward turn as it gets closer to the mountain range, in response to the effects of the stronger northerly wind over the mountain due to the effects of channeling flow. The vortex may deflect southward when approaching a longer mountain range and then rebound northward upstream of the mountain ridge. The southward deflection is primarily induced by the convergence (stretching) effect due to the combination of the speedy core at the southwestern flank of the vortex and a northerly jet between the vortex and the mountain. The vortex then rebounds northward to pass over the mountain as the speedy core rotates counterclockwise to the eastern flank of the vortex. The track deflection near the mountain is also affected as either of both physics is deactivated.

Sensitivity experiments show that for a given steering flow and mountain height, a linear relationship exists between the maximum upstream deflection distance and the nondimensional parameter R_{mw}/L_y , where R_{mw} is the vortex size (represented by the radius of the maximum wind) and L_y is the north–south length scale of the mountain. The southward deflection distance increases with smaller R_{mw}/L_y and higher mountains for both weaker and stronger steering flow. When the steering-flow intensity is doubled, the southward deflection is roughly reduced by 50%.

1. Introduction

Various mountains may exert a wide range of modifications on impinging tropical cyclones, including track deflection, translation speed change, and looping paths of the cyclones. Among various scenarios of the mountain impacts, the vortex past an isolated mountain has

been widely investigated using observations and numerical models (e.g., Brand and Brelloch 1974; Wang 1980; Chang 1982; Bender et al. 1987; Zehnder 1993; Yeh and Elsberry 1993a,b; Zehnder and Reeder 1997; Lin et al. 1999, 2005; Kuo et al. 2001; Huang and Lin 2008; Jian and Wu 2008; Huang et al. 2011; Lin and Savage 2011; Hsu et al. 2013; Wu et al. 2015). In reality, as one of the examples, a mesoscale mountain range—namely, the Central Mountain Range (CMR)—is located in Taiwan, which rises to about 3.5 km in height and stretches approximately 300 km from north-northeast to south-southwest and is about 100 km wide. Such an island mountain provides an ideal setting for studying the vortex track deflection (e.g., Yeh and Elsberry 1993a,b; Lin et al. 1999; Huang et al. 2011; Wu

 Denotes Open Access content.

Corresponding author address: Prof. Ching-Yuang Huang, Dept. of Atmospheric Sciences, National Central University, No. 300, Jhongda Rd., Jhongli City, Taoyuan County 32001, Taiwan.
E-mail: hcy@atm.ncu.edu.tw

DOI: 10.1175/JAS-D-15-0218.1

et al. 2015) but also offers difficulties in constructing the map of track deflection for impinging typhoons owing to the complexity in the combination of many possible factors involved in the deflection.

A particular scenario of the track deflection in the above pertains to the advection of a dry vortex toward the center of a mountain barrier at a right angle. Based on the systematic experiments using a primitive equation (PE) model without surface friction and planetary boundary layer (PBL) turbulent mixing, Lin et al. (2005) found that the upstream track deflection for a vortex approaching a mountain is mainly dominated by three nondimensional controlling parameters: V_{\max}/Nh (the vortex Froude number), U/Nh (the basic-flow Froude number), and R_{mw}/L_y (the nondimensional vortex size), where N is the environmental stability frequency and h is the mountain height. These nondimensional parameters are formed from eight possible dimensional parameters including U (the basic-flow speed), V_{\max} (maximum tangential wind of the initial vortex), f (the Coriolis parameter), L_x (the mountain length scale in the direction of the vortex movement), L_y (the mountain length scale in the direction normal to the vortex movement), R_{mw} (the radius of V_{\max}), N , and h . The basic-flow Froude number was found to play no major role in the direction of track deflection but influenced significantly the degree of deflection. Because of the nature of a mesoscale vortex at a relatively shorter time scale as passing over a mesoscale mountain similar to Taiwan topography, the Rossby number (U/fL) that measures the rotation effects also does not play a significant role in the track deflection. Track deflection and degree of the deflection with respect to the control parameters have also been investigated by Huang and Lin (2008) using a shallow-water (SW) model. In general, both PE and SW studies indicate that the control parameter (R_{mw}/L_y) is most important for predicting the track deflection. The vortex tends to be deflected leftward (facing downstream) as it is approaching the mountain barrier with smaller R_{mw}/L_y . This has been explained by the strong terrain blocking with northerly faster wind ahead of the mountain (Lin et al. 2005) to drive the vortex southward. In a recent study (Wu et al. 2015), the southward track deflection prior to landfall has been explained by the stronger midtropospheric channeling effects as an ideal intense vortex moves close to a short mountain range. The mechanism of the induced track deflection prior to passage over the terrain should be further investigated in regard to a variety of vortex sizes and intensities as well as mountain ranges. In addition, the response of the track deflection with respect to these parameters has not been investigated in systematic experiments for the cyclones with more

complete physics including boundary layer turbulent mixing and cloud effects.

In this paper, we will focus on the simple case with an idealized westbound cyclone past a mountain range at various lengths and will further look into the potential control parameters for upstream track deflection. A comprehensive idealized WRF Model is applied in this study to investigate the associated mechanism of induced southward deflection and the relationship of the track deflection with respect to the control parameters. For completion of the major physics, the PBL with a surface-layer lower boundary has been included. In this study, in order to simplify the dynamics, we will not consider the beta effects as it will introduce additional beta drift to the vortex motion (e.g., Chan and Williams 1987; Smith 1993) that would complicate track deflection of a vortex impinging the mountain barrier.

In section 2, the numerical aspects including the idealized WRF Model and vortex initialization will be introduced. In section 3, we will show the experimental results to identify the track deflection of a vortex past various mountain ranges. We will investigate the mechanism for the upstream track deflection for different vortices. Influences of boundary layer turbulent mixing and cloud effects on the upstream track deflection are also discussed. Based on the results of systematic experiments in this study, the relationship between the maximum upstream deflection distance and the potential nondimensional parameter (R_{mw}/L_y) is constructed in section 3. Finally, we give our concluding remarks in section 4.

2. Numerical aspects

a. The numerical model

The Weather Research and Forecasting (WRF) Model, version 3.3.1 (<http://wrf-model.org/index.php>; Skamarock et al. 2008), is employed for our idealized simulations. The WRF Model is nonhydrostatic in terrain-following coordinates. The vertical model domain employs 41 vertically stretched grids topped at 20-km height. The model simulations in section 3 include the Yonsei University (YSU) PBL parameterization (Hong et al. 2006), the WRF single-moment 6-class graupel cloud microphysics (WSM6) (Hong and Lim 2006) and the modified Tiedtke cumulus parameterization (Tiedtke 1989). Radiative effects are not included in the simulations.

All simulations conducted in this study are considered on a constant- f plane at 23°N. A tropical thermal sounding shown in Fig. 1, similar to the mean tropical sounding (Jordan 1958), is used for model initial conditions that are assumed to be horizontally homogeneous. The sounding

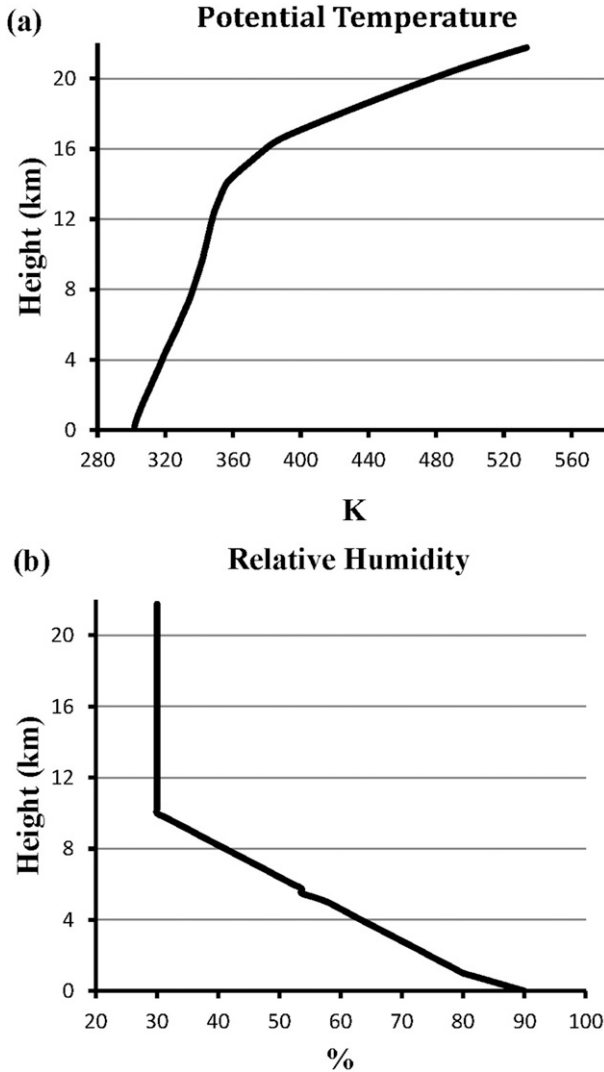


FIG. 1. The vertical profile of the model initial sounding for (a) potential temperature (K) and (b) relative humidity (%).

is conditionally stable with the specified reference relative humidity (RH) that linearly decreases with height from 90% near the surface to 80% at 1 km and then to 30% at 10 km above which a constant RH of 30% is assumed. A tiny kink in the RH profile near 5-km height is induced as a result of the hydrostatic adjustment with the sounding profile of unchanged potential temperature. With the prescribed homogeneous environmental wind and moisture, the steering-flow condition can be solved from a thermal-wind balance. Given the virtual temperature $T_v = T(1 + 0.608q)$, where T is temperature (K) and q is the water vapor mixing ratio (kg kg^{-1}), the thermal wind balance requires

$$-g \frac{\partial \ln T_v}{\partial y} - R \frac{\partial T_v}{\partial z} \frac{\partial \ln p}{\partial y} = f \frac{\partial U}{\partial z}, \quad (1)$$

where U is the zonal geostrophic wind speed and the horizontal derivatives are taken at constant height z . Using the virtual potential temperature $\theta_v = T_v(p_0/p)^{R/c_p}$, where p_0 is 1000 hPa, (1) can be expressed as

$$-g \frac{\partial \ln \theta_v}{\partial y} - R \left(\frac{g}{c_p} + \frac{\partial T_v}{\partial z} \right) \frac{\partial \ln p}{\partial y} = f \frac{\partial U}{\partial z}, \quad (2)$$

where the sum in the parentheses indicate the static stability of moist air. Thus, for constant easterly geostrophic wind in Northern Hemisphere, there are corresponding positive meridional pressure gradient ($\partial p / \partial y > 0$) and positive meridional virtual temperature gradient ($\partial T_v / \partial y > 0$) but with a negative meridional virtual potential temperature gradient ($\partial \theta_v / \partial y < 0$) for a normal stable environment ($\partial T_v / \partial z < 0$ and $g/c_p + \partial T_v / \partial z > 0$).

During the WRF Model integration, open boundary conditions are specified at all the lateral boundaries, while a sponge layer of 4 km is imposed at the top to absorb the reflected waves from the upper boundary. The initial sea surface temperature (SST) is set to 300.15 K and is fixed during the 96-h model integration. The initial potential temperature near the surface is slightly warmer than that at the surface. This stable surface layer prevents the vortex from rapidly developing through the convective instability.

b. Vortex initialization

The offline, static vortex initialization scheme, which was developed by Nolan (2011) and also used by Stern and Nolan (2011), is applied in this study. The scheme assumes that the vortex is axisymmetric and in gradient-wind balance with the maximum tangential wind speed V_{\max} at the radius R_{mw} . The radial profile of the tangential wind is a modified Rankine vortex, which decays as a Gaussian with height as described in Stern and Nolan (2011). Thus, for any specified vortex the initial tangential wind does not become anticyclonic at upper levels. Given a horizontally homogeneous wind profile the environment of the vortex is computed from the thermal-wind balance. Then, the balanced static vortex and environment provide the initial conditions for a WRF simulation.

Note that turbulent mixing in the PBL is not included in the offline, static vortex initialization, while it is included in WRF simulations. Once the initial conditions are imported into WRF, the model would take some time to create the Ekman flow in the boundary layer. Thus, our experimental design ensures that the initial vortex is away from a prescribed mountain far enough so that the vortex intensity does not vary considerably before approaching the mountain. We found that after 9 h of integration the Ekman flow in the PBL far upstream from

TABLE 1. The numerical experiments for an ideal cyclonic vortex with varying maximum tangential wind speeds V_{\max} at the radii R_{mw} past an isolated mountain at a peak of $h = 3500$ m with different east–west and north–south elongation terrain parameters $L_x = 100$ km and $L_y = 300$ km, respectively. The steering flow U is easterly wind of -4 m s $^{-1}$. The initial vortex center is located at grid (185, 151) and the mountain peak is located at grid (135, 150). Both boundary layer turbulent mixing and cloud microphysics are included in the model simulations.

R_{mw} (km)	V_{\max} (m s $^{-1}$)			
	20	25	30	35
100	U1V1R1	U1V2R1	U1V3R1	U1V4R1
150	U1V1R2	U1V2R2	U1V3R2	U1V4R2
200	U1V1R3	U1V2R3	U1V3R3	U1V4R3
250	U1V1R4	U1V2R4	U1V3R4	U1V4R4

the translating vortex changes the direction less than 1 $^\circ$ until the end of the simulation.

c. Experiment setup

The experiments in this study are described in Tables 1–3. As shown in Fig. 2, two nested domains with resolutions of 15 and 5 km for domains 1 and 2, respectively, are employed for the experiments in Tables 1 and 2. The experiments in Table 3 are designed for investigating track sensitivity to terrain parameters for longer mountain ranges and apply a single domain with 15-km resolution. In all experiments, the mountain barrier is prescribed by a Gaussian function as

$$H(x, y) = h \exp \left[-\frac{(x - x_m)^2}{\sigma_x^2} - \frac{(y - y_m)^2}{\sigma_y^2} \right], \quad (3)$$

where x_m and y_m are the x and y locations of the mountain peak; the height of the mountain peak is h , and σ_x and σ_y are the length scales at e -folding distance, corresponding to the given reference lengths L_x (width) and L_y (length) in the x and y directions, respectively. The value of L_y indicates the location of the mountain

TABLE 2. As in Table 1, but for the steering flow U of -8 m s $^{-1}$. The initial vortex center is located at grid (233, 151) and the mountain peak at grid (135, 150).

R_{mw} (km)	V_{\max} (m s $^{-1}$)			
	20	25	30	35
100	U2V1R1	U2V2R1	U2V3R1	U2V4R1
150	U2V1R2	U2V2R2	U2V3R2	U2V4R2
200	U2V1R3	U2V2R3	U2V3R3	U2V4R3
250	U2V1R4	U2V2R4	U2V3R4	U2V4R4

that flats to about $\exp(-5)$ of the maximum height. The specification of $L_x = 100$ km corresponds to $\sigma_x = 22.36$ km and $L_y = 2000$ km corresponds to $\sigma_y = 223.60$ km, and other sets can be linearly inferred. For the surface type of each grid point, it is defined as a land surface if the surface elevation is higher than 1 m; otherwise, it is defined as a water surface. The specification of the surface type provides a coastline as shown in Fig. 2 for one example of topography (with $h = 3500$ m, $L_x = 100$ km, and $L_y = 300$ km). In this study, a simple uniform easterly steering flow is considered for specified different initial vortices and terrain configurations. Under this uniform steering flow, a cyclone east of the central mountain moves westward toward the center of the island mountain.

3. Results and discussion

a. The initial vortex and evolution

Figure 3 shows that the model pressure perturbations and potential temperature at the surface level at the initial time for the ocean-only experiment with an initial moderate vortex ($V = 35$ m s $^{-1}$). Initially, the vortex possesses a very cold core at the surface because the initial wind is maximized at $z = 1500$ m. Note that a warm core is presented above the height of maximum tangential wind at 850 hPa. It is noted herein that as indicated by (2) the environmental meridional potential

TABLE 3. The numerical experiments for an ideal cyclonic vortex with $V_{\max} = 20$ m s $^{-1}$ and $R_{\text{mw}} = 80$ km past various mountain ranges with different mountain peaks h and north–south elongation terrain parameters L_y , where H1–H5 denotes 1500–3500 m and L1–L6 denotes 1000–3500 km. The east–west elongation scale of the mountain L_x is fixed as 100 km (W1). The steering flow U is easterly wind of -4 m s $^{-1}$. The initial vortex center is located at grid (185, 151) and the mountain peak at grid (135, 150). Both boundary layer turbulent mixing and cloud effects are included in the model simulations.

h (m)	L_y (km)					
	1000	1500	2000	2500	3000	3500
1500	W1L1H1	W1L2H1	W1L3H1	W1L4H1	W1L5H1	W1L6H1
2000	W1L1H2	W1L2H2	W1L3H2	W1L4H2	W1L5H2	W1L6H2
2500	W1L1H3	W1L2H3	W1L3H3	W1L4H3	W1L5H3	W1L6H3
3000	W1L1H4	W1L2H4	W1L3H4	W1L4H4	W1L5H4	W1L6H4
3500	W1L1H5	W1L2H5	W1L3H5	W1L4H5	W1L5H5	W1L6H5

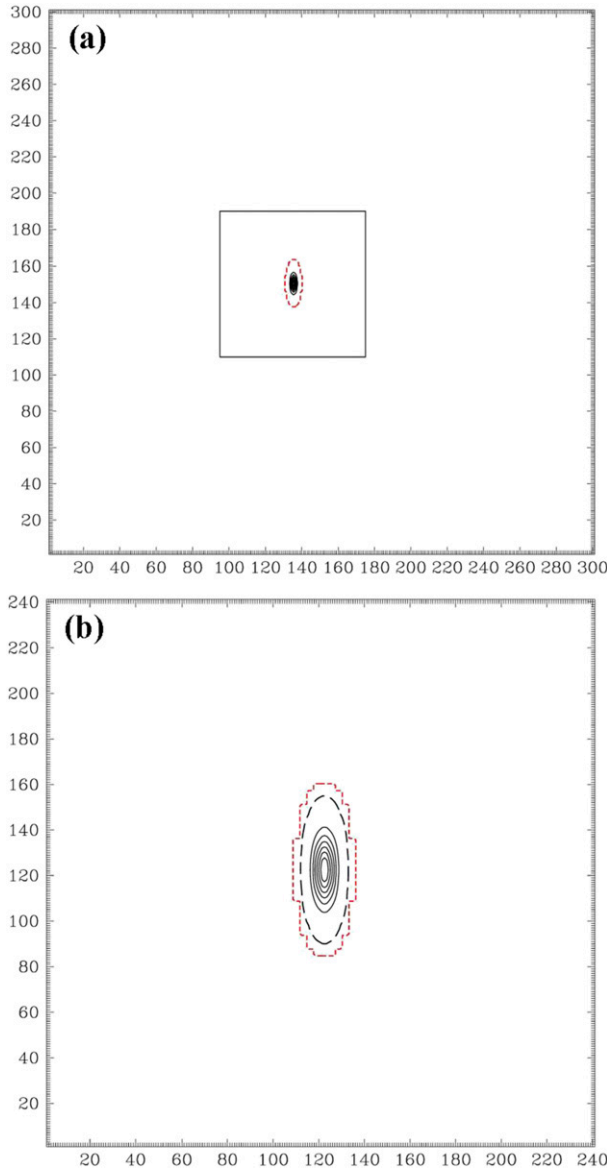


FIG. 2. (a) The model domains consisting of 301×301 grid points in the coarse domain with 15-km resolution and 241×241 grid points in the fine domain with 5-km resolution and (b) the terrain height in the fine domain with the coastline (shorter dashed in red) and 10-m height (longer dashed in black) included. The terrain heights at a contour interval of 500 m use $L_x = 100$ km and $L_y = 300$ km with the peak height of 3500 m at (135, 150) in the coarse domain.

temperature gradient is negative in association with the positive meridional pressure gradient, under the stable environmental condition without vertical wind shear.

In the ocean-only case, the simulated weaker vortex translates almost straight westward within a reasonable period of time. However, an initial stronger vortex tends to slightly deflect northward as the vortex begins to

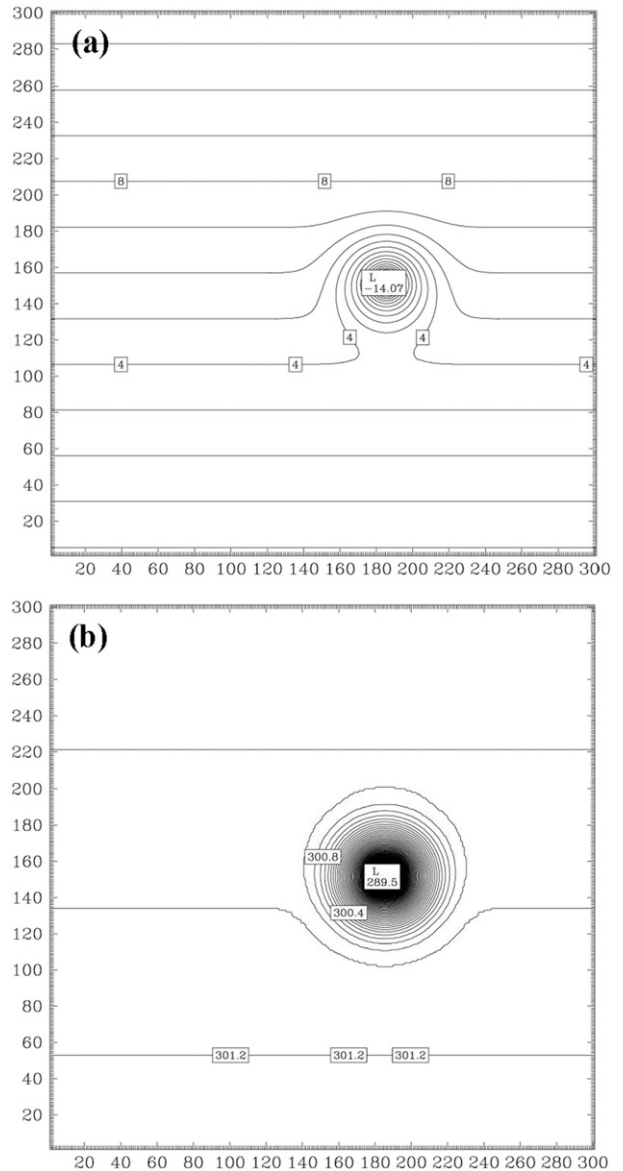


FIG. 3. (a) Pressure perturbation (hPa) at the surface at the coarse domain at the initial time. (b) As in (a), but for potential temperature (K). The contour intervals are 0.5 hPa for pressure and 0.1 K for potential temperature with a cold core.

develop strong asymmetric convection at later times (as shown later). It has been shown that some of idealized vortex translations may slightly deflect northward (or rightward) (e.g., Yeh and Elsberry 1993a,b; Huang et al. 2011; Wu et al. 2015). Such a northward deflection has been attributed to some possible reasons—for example, the effects of boundary layer turbulent mixing that cause the development of asymmetric circulation (Yeh and Elsberry 1993b). According to (2), it will be colder to the north of the cyclone than to the south as seen in Fig. 3 despite that the meridional potential temperature

gradient is small, thus favoring stronger air–sea interaction to the north due to larger air–sea temperature differences [see further discussion of this effect in Nolan (2011)]. The vortex can propagate straight downstream without deflection in a very long travel time when it is not developing into an intense cyclone. In this sense, we will thus limit this study to moderate cyclones (see Tables 1–3) for reducing the uncertainty involved in track deflection with respect to the hypothesized parameters. For exploring channeling effects and physical processes in relation to upstream track deflection, we have also used a more intense vortex.

b. Time evolution of the vortex intensity

Figure 4 shows time evolution of the maximum horizontal wind speed within a 300-km radius of the vortex center on the coarse domain for the experiments in Table 1 with an island mountain similar to Taiwan topography. For both slower steering flow U1 (4 m s^{-1}) and faster steering flow U2 (8 m s^{-1}), the vortex center makes landfall at about 51 h; the initial vortex is put at a distance 2 times away from the mountain in the faster steering flow. During the earlier period when the vortex is still somewhat away from the mountain, the vortex intensity slightly decays with time. The decaying rates are similar for both steering flows, regardless of vortex size. We note that the vortex does not become intensified with time, given the specified RH in the mid-troposphere and potential temperature at the surface layer slightly warmer than the SST. After the first period (about 24 h), the vortex is more influenced by topographic effects with different responses in different experiments and steering flows. Interestingly, the topographic influence on the developing vortex intensity is earlier for initial stronger vortices. Such influence is delayed to about 42 h for stronger steering flow, except for the strongest-vortex experiments (i.e., U2V4Rx series).

There are various and complicated responses in the vortex intensity in the second period with respect to different vortex sizes and intensities when the vortex has strongly interacted with the topographic effects. However, there is no significant reduction or increase in the vortex intensity as the vortex remains east of the mountain by about 54 h. In addition, the relative changes in vortex intensity at this stage for different vortex sizes, intensities, and steering flows are not large. The temporal variations of the vortex intensity are relatively larger for initial stronger vortices, regardless of steering flow. None of the cyclones tend to rapidly develop with time at the second stage and the third stage that the vortex is departing from the island (about 54–60 h). Prevention of a rapid change in cyclone intensity (and

size) at the first and second stages helps investigate the track evolution of a moderate vortex past different mountain ranges with respect to some hypothesized parameters for different scenarios in the experiments that will be discussed later.

c. Track sensitivity to steering flow, vortex intensity, and size

Vortex movement under faster- and slower-steering flows in the presence of an isolated mountain is investigated with respect to varying maximum tangential wind V_{\max} and its radius R_{mw} . Both boundary layer turbulent mixing and cloud effects (from cloud microphysics and cumulus parameterization) are included in the sensitivity experiments with two nested domains as shown in Fig. 2. Since the vortex upstream of and near the mountain is mainly concerned, an outer domain size with 301×301 grids is employed. The terrain herein represents Taiwan topography with a peak height of 3500 m.

The simulated vortex tracks for the slower easterly steering flow (at a speed of 4 m s^{-1}) are shown in Fig. 5 with the panel arrangement corresponding to Table 1. The vortex center is defined as the location of minimum surface pressure perturbation. With boundary layer turbulent mixing and cloud effects included, these vortices only slightly change their intensities with time as shown in Fig. 4, but their inner cores get more concentrated at later times when they are close to the mountain. As can be seen from the evolving tracks, there is little track deflection at the earlier stages when the cyclonic circulation of the vortex is still far away from the mountain, except for some southward deflection associated with the larger cyclones ($R_{\text{mw}} = 200$ and 250 km) at the weakest intensity ($V_{\max} = 20 \text{ m s}^{-1}$) (see cases U1V1R3 and U1V1R4). We find that the vortex may keep a similar size and intensity as it is not close to the mountain. As the cyclones are further approaching the mountain, there is slightly northward deflection, especially for weaker cyclones. Near landfall, the smaller cyclones (e.g., the R1 series) seem to deflect southward. The tracks then tend to move northward of the centerline after passing over the mountain but rebound somewhat southward at later times.

Fixing the initial cyclone intensity, the increase in vortex size seems to exhibit an earlier southward track but followed by a northward track and then a southward track prior to landfall. Fixing the cyclone size, the increase in vortex intensity seems to reduce the upstream northward track deflection. The southward rebound prior to landfall becomes more evident for the smallest cyclones. This agrees with some observed slowly moving typhoons [e.g., Haitang (2005) and Krosa (2007)] that

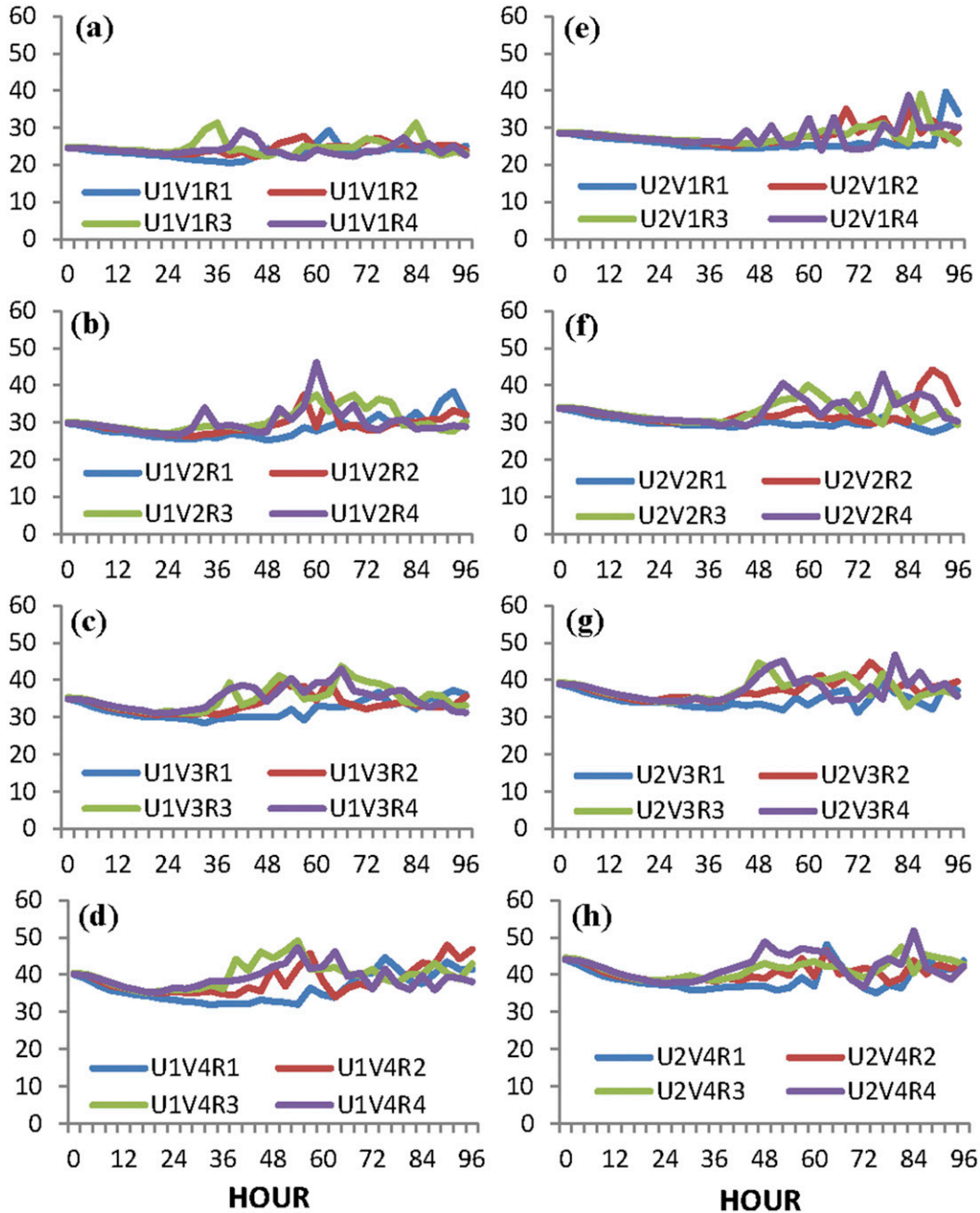


FIG. 4. Time evolution of the maximum horizontal wind speed (m s^{-1}) within the 300 km of the vortex center at the coarse domain for the experiments in Table 1: (a) U1V1R1–R4, (b) U1V2R1–R4, (c) U1V3R1–R4, and (d) U1V4R1–R4 for slower easterly steering flow U1 (4 m s^{-1}). (e)–(h) As in (a)–(d), respectively, but for faster easterly steering flow U2 (8 m s^{-1}).

exhibit a looping track with southward deflection near-
ing landfall.

For easterly steering flow increased to 8 m s^{-1} , the tracks exhibit less upstream deflection than seen in Fig. 6, except for some earlier southward deflection associated with the larger but weaker cyclones (e.g.,

U2V1R3 and U2V1R4). Note that the initial vortex in these faster-steering-flow experiments is specified farther upstream so that the vortex makes landfall at approximately the same time as for the slower steering flow. As the initial vortex becomes larger, it would experience the terrain effects earlier owing to its outer

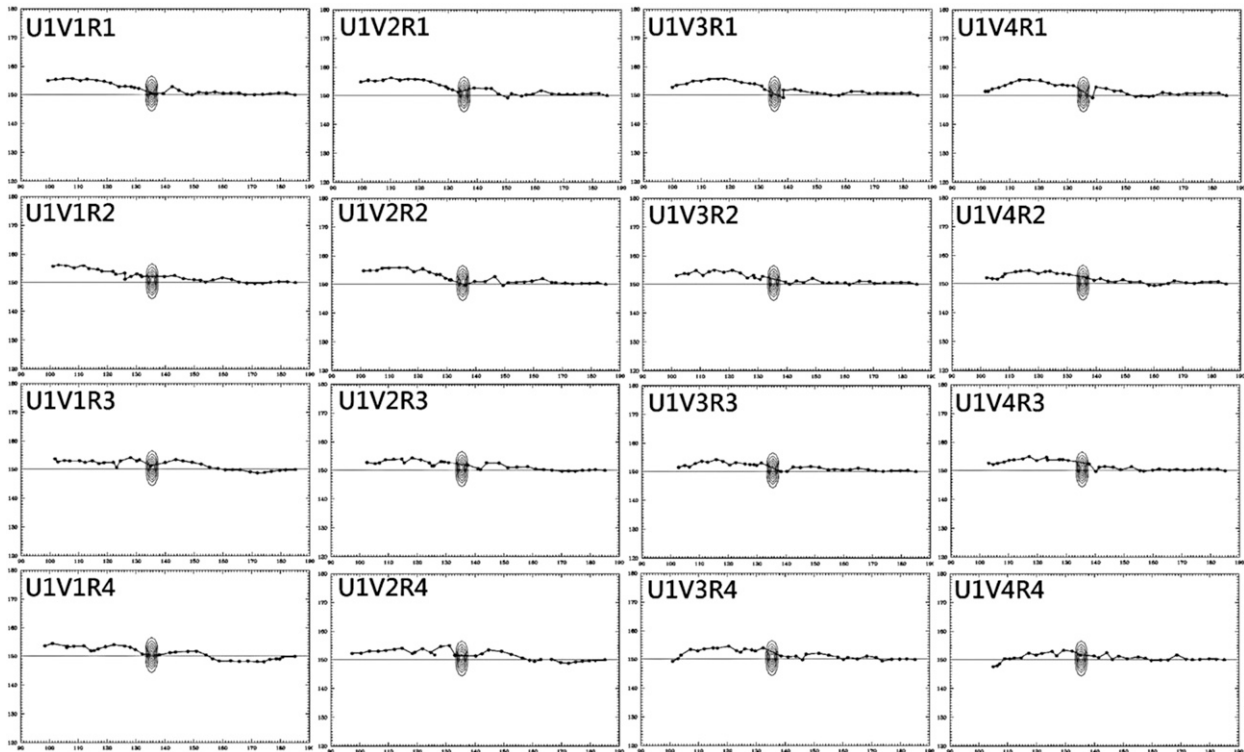


FIG. 5. The evolution of vortex center every 3 h defined as the location of minimum surface pressure perturbation. The steering flow is easterly at 4 m s^{-1} . The contours represent the terrain height at an interval of 500 m (zero-value contours and coastlines are not plotted). Arrangement of the panels corresponds to that of the experiments in Table 1. The x and y coordinates are from grids 90 to 190 and from 120 to 180, respectively, labeled every 10 grid points, with an interval of 15 km.

expansion of the swirling flow. However, such an impact seems to be offset by the increased intensity of the cyclone (see the bottom panels). In general, the track under the stronger steering flow is less influenced by the mountain as compared to the weaker steering flow in agreement with other studies (e.g., Yeh and Elsberry 1993a,b; Huang and Lin 2008; Wu et al. 2015). The southward rebound of the vortex nearing landfall is significantly reduced or disappears for this short mountain range.

d. Track deflection: Channeling effects

Some of the vortex tracks exhibit a salient southward deflection near the mountain for a stronger vortex (e.g., in U1V3R1 and U1V4R1). The southward track deflection near the mountain has been attributed to the effects of channeling flow as the intense vortex core gets confined east of the mountain slope and develops stronger northerly wind (Lin et al. 2005; Huang et al. 2011; Wu et al. 2015). Flow channeling can result at the time when the vortex starts to strongly interact with the effects of mountain blocking. Figure 7 shows the vortex circulation at the height of 1 km and the associated 12-h precipitation on the fine domain at 42 and 48 h for U1V4R1. The vortex moves almost straight westward at

the early stage but tends to deflect slightly northward after about 36 h (also see Fig. 5) and has developed stronger flow at the first quadrant and some of the fourth quadrant of the vortex at 42 h (Fig. 7a). The enhanced cyclonic flow at 3-km height in these regions is not as strong as at 1-km height (figure not shown). At both heights, the stronger flow prevails at the northeastern and eastern flanks of the vortex, which consistently supports a northward deflection of the vortex. Larger rainfall (more than 200 mm in 12 h) mainly at the fourth quadrant is also produced in association with the stronger wind. The dominant rainfall at this quadrant can be attributed to the fact that the outer swirling flow of the vortex after passing around the southern island tends to converge with the inner vortex flow to the southeast of the vortex center. The region of stronger vortex flow tends to rotate counterclockwise with time and displays an extension of enhanced northerly wind along the east slope of the mountain at 48 h due to the effects of channeling flow. The vortex track deflects somewhat southward as the vortex is closer to the mountain base from 51 to 54 h and then passes over the mountain peak and keeps a roughly westward movement. The vortex center when defined as the

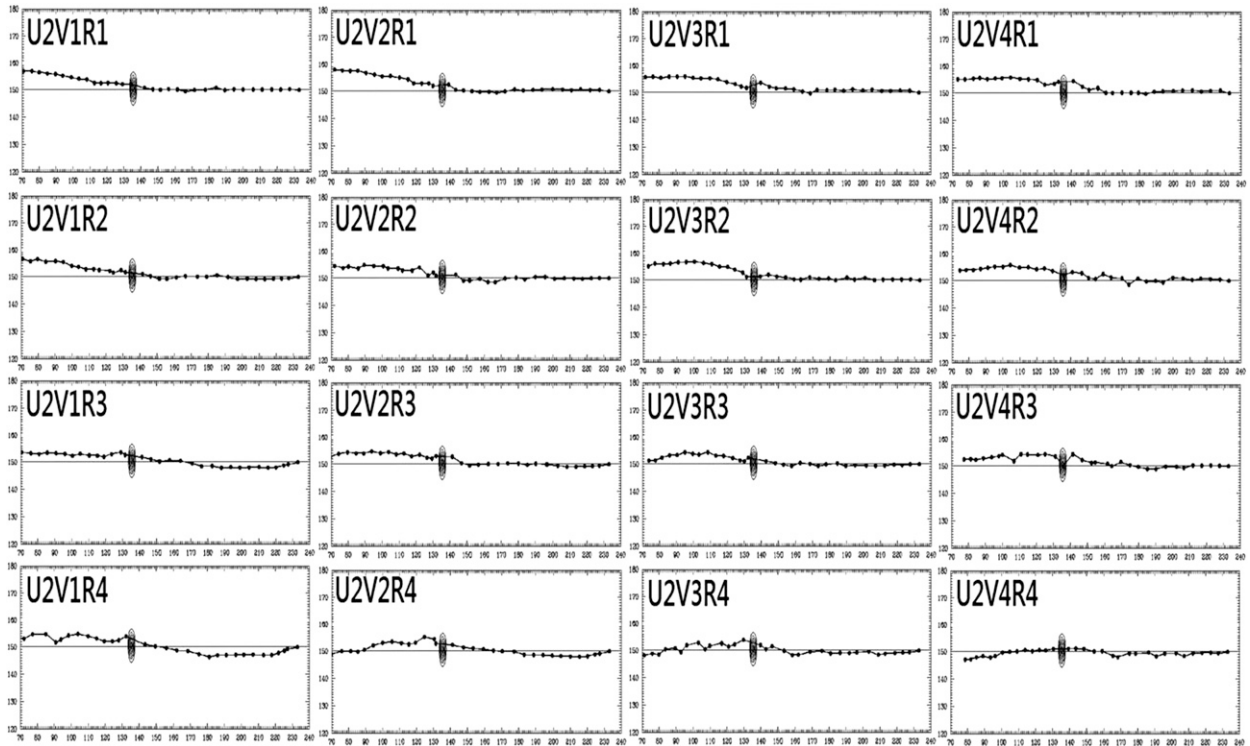


FIG. 6. As in Fig. 5, but for the stronger easterly flow of 8 m s^{-1} . Arrangement of the panels corresponds to that of the experiments in Table 2.

circulation center is closer to the central mountain so that the vortex track appears less southward.

We further examine the vertical development of the enhanced wind speed in the vortex. Figure 8 shows the circulation at the east–west cross section through the vortex center at 48 and 51 h for U1V4R1. At 42 h, the stronger wind (mostly southerly) dominates at lower levels at the eastern flank of the vortex in association with stronger updrafts (about 3 m s^{-1}) that develop to about 9-km height (figure not shown). At 48 h, the eyewall structure is evident at the eastern flank of the vortex associated with the strong updrafts that roughly follow the isotherms of equivalent potential temperature. Stronger wind east of the vortex center remains below 2-km height, while faster wind speed is also present farther outward below about 9-km height in the outer vortex. At this time, the faster wind at the western flank of the vortex has been induced along the eastern slope and extends upward to about 9-km height. The wind enhancement below 2-km height near the mountain base (about 30–50 km in Fig. 8a) is mainly associated with the stronger northerly flow. The enhanced wind zone is also extended upward along the mountain slope and reaches to about 6-km height. As the vortex moves closer to the mountain base at 51 h, such wind speed enhancement is also extended upward to 9-km height over the mountain

(Fig. 8b), with the strongest northerly wind component at about 6-km height (figure not shown). In the presence of the high mountain range, the cyclonic flow of the upper vortex over the mountain accelerates southward along the mountain range.

In ideal experiments with an initial intense vortex (with the maximum wind speed over 75 m s^{-1}), Wu et al. (2015) found that the northerly wind component may be more enhanced in the midtroposphere owing to the effects of channeling flow, which cause the vortex to deflect southward before passing over the mountain range. The U1V4R1 experiment uses an initial moderate vortex (with the maximum tangential wind speed of 35 m s^{-1}) past a relatively shorter mountain range. The developed maximum wind speed of the vortex is only about 50 m s^{-1} . To further compare the effects of channeling flow for a stronger vortex past a similar mountain range, we further reduce the vortex size R to 80 km, increase the initial vortex intensity V to 50 m s^{-1} , and enlarge the length of mountain range L_y to 400 km, denoted by the experiment WL400. The topography of the mountain range with $L_y = 400 \text{ km}$ in WL400 is similar to that in Wu et al. (2015). Figure 9 shows the vortex circulations and horizontal wind speed for WL400 at the time when the vortex is close to the mountain. The vortex gradually deflects northward, with

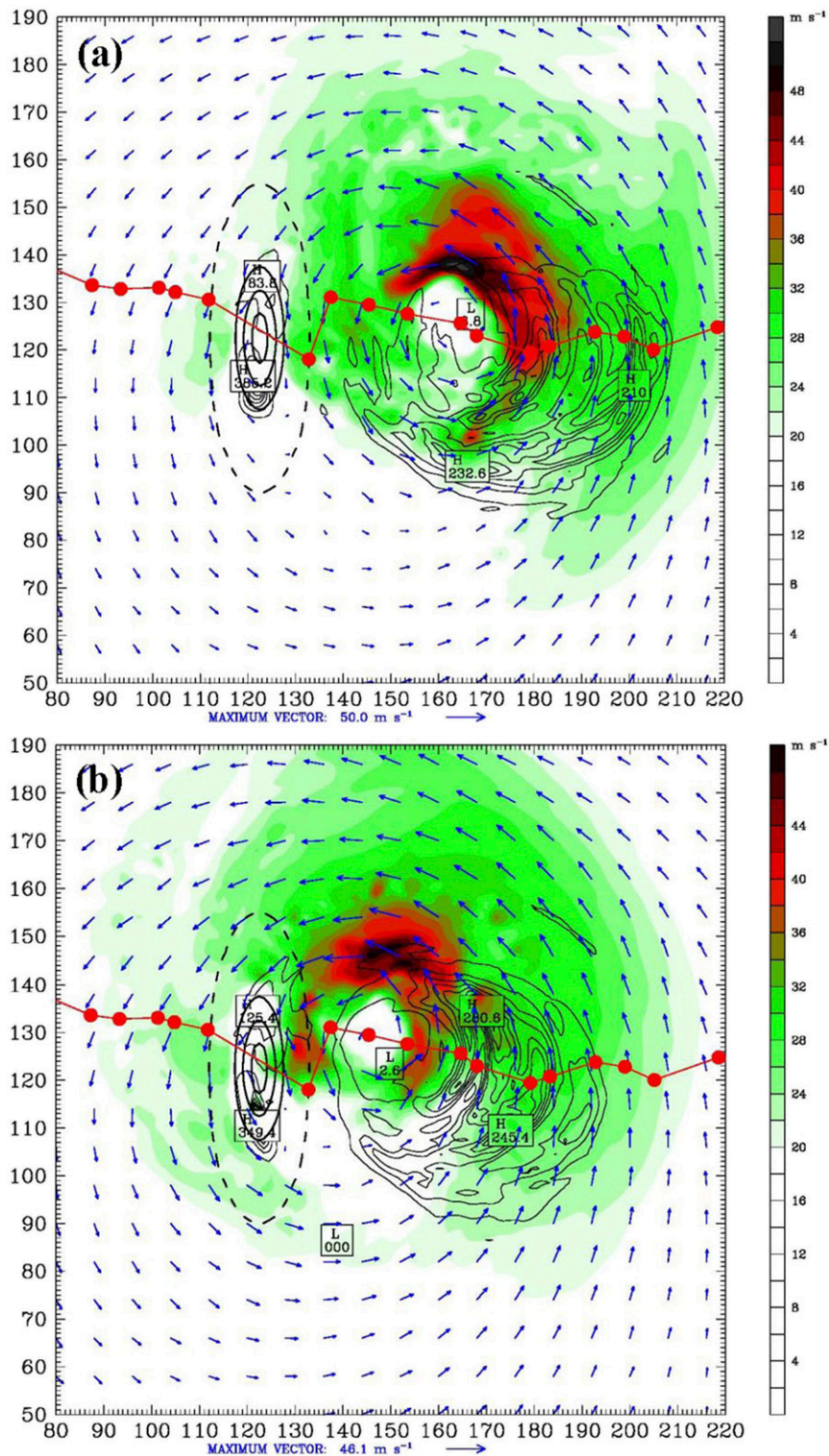


FIG. 7. (a) Horizontal wind vector and wind speed (shaded, m s^{-1}) and 12-h precipitation (thin contours at an interval of 30 mm) at the fine domain for U1V4R1 at the height of 1 km at 42 h. (b) As in (a), but at 48 h. Solid thick contours are for 1-, 2-, and 3-km terrain heights, and dash contours are for 10-m height. The red line with dots is the vortex track every 3 h.

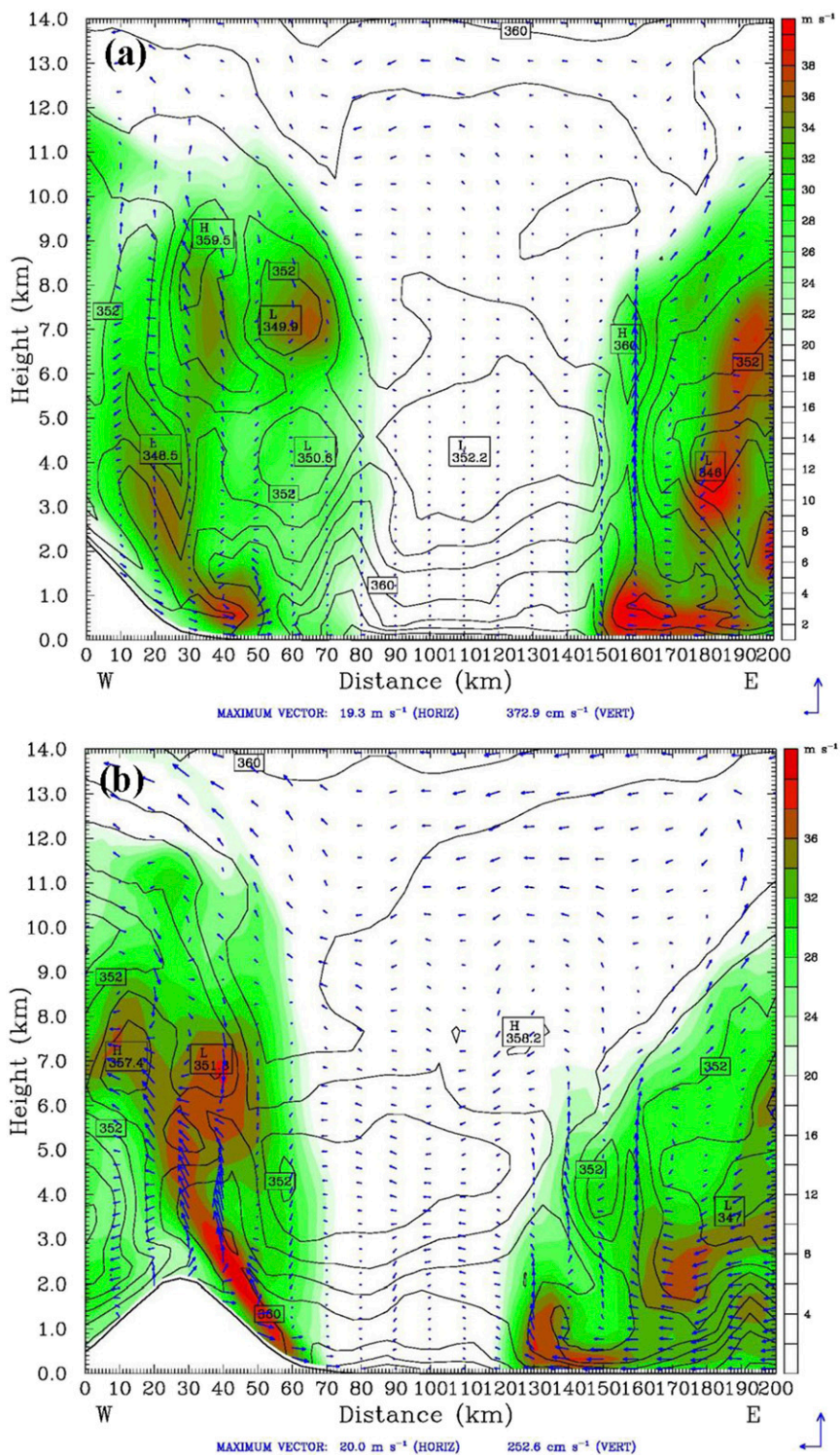


FIG. 8. The equivalent potential temperature (contours, interval of 2 K), horizontal wind speed (shaded, m s^{-1}), and wind vector at the x - z cross section through the vortex center at the fine domain for U1V4R1 at (a) 48 and (b) 51 h.

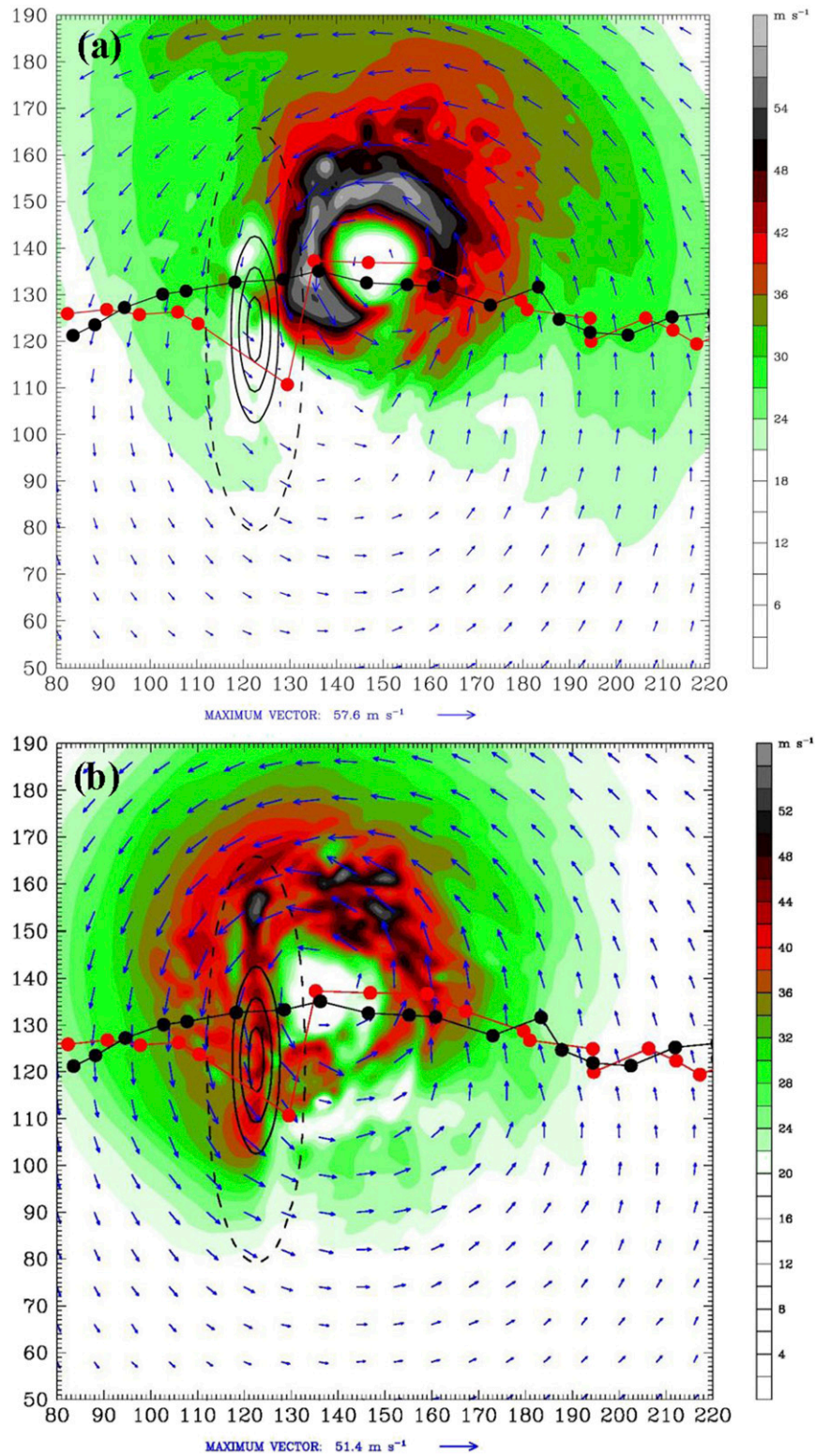


FIG. 9. Horizontal wind vector and wind speed (shaded, m s^{-1}) at the fine domain for WL400 at the height of (a) 1 km at 48 h and (b) 5 km at 51 h. The contours represent the terrain heights as in Fig. 7. The red line with dots is the vortex track every 3 h, and the black line with dots in (a) and (b) is the vortex track every 3 h in the ocean-only case.

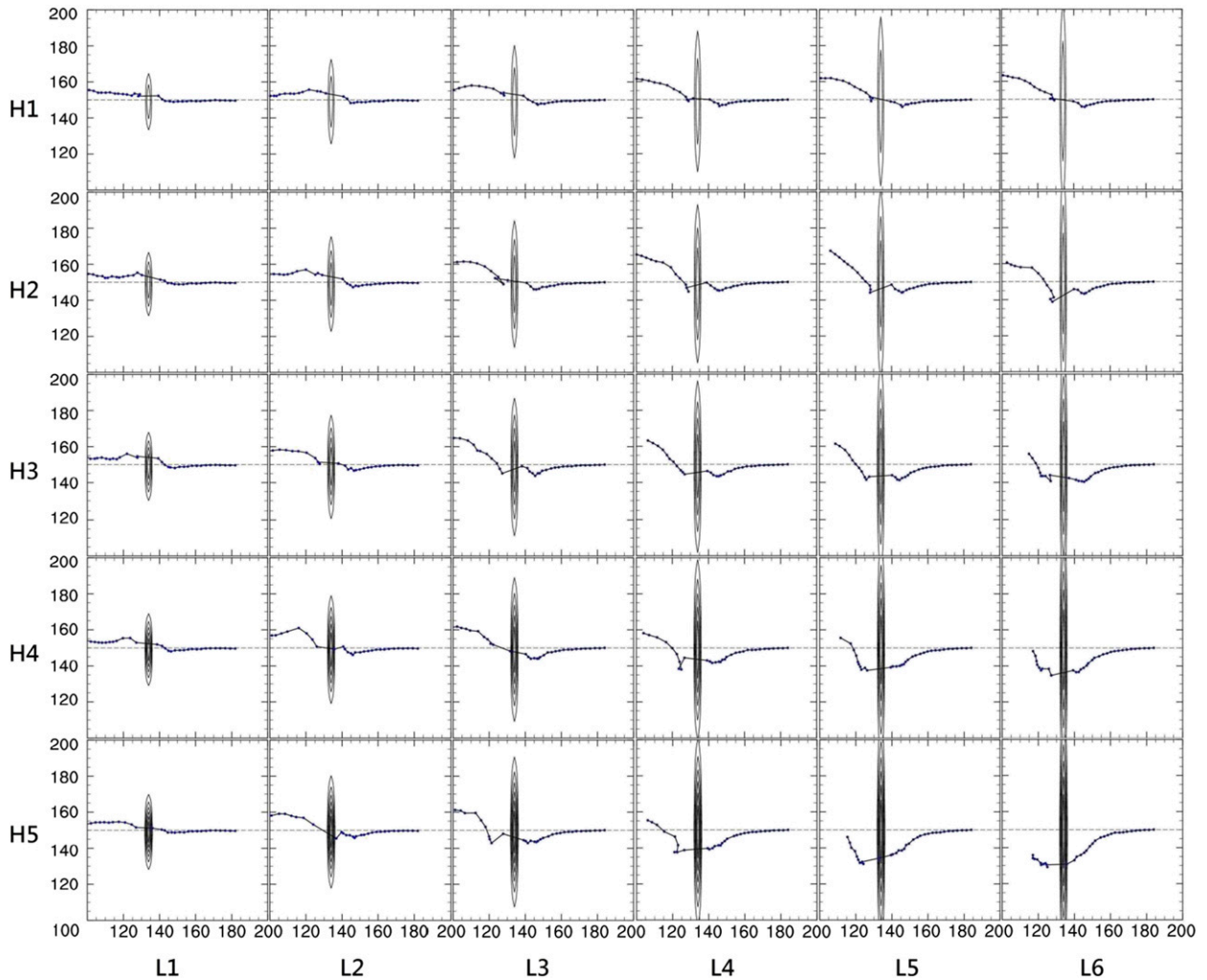


FIG. 10. The evolution of vortex center every 3 h defined as the location of minimum surface pressure perturbation. The contours represent the terrain height at an interval of 500 m (zero-value contours and coastlines are not plotted). Arrangement of the panels corresponds to that of the experiments in Table 3.

the largest deflection of about 80 km in 45–51 h (Figs. 9a,b). As in U1V4R1, the northward track deflection at the earlier stage is accompanied by the stronger southerly wind and larger rainfall rates (over 300 mm day^{-1}) at the southeastern and eastern flanks of the vortex (figures not shown). Compared to the slightly northward track in the ocean-only case (denoted by the black line with dots), the northward deflection is slightly enhanced in the presence of the mountain range. We found that in the ocean-only case the slightly northward deflection of the vortex undergoes with more precipitation produced at the southeastern and eastern flanks of the vortex, in response to the enhanced outer southerly flow southeast of the vortex. We also found that this northward deflection may start at a later time with the less-developed convection for an initial weaker vortex.

Similar to U1V4R1 (with a shorter mountain length), the channeling flow northeast of the mountain in WL400 is significantly enhanced at both heights, but the flow enhancement is stronger at 1-km height (Fig. 9a) than at 3-km height (figure not shown). As in U1V4R1, the vortex is not ready for taking a south turn at this time (48 h) even in the presence of such localized strong northerly wind. The vortex center near the surface then is suddenly pushed southward along the east coast from 51 to 54 h, with a maximum southward deflection of 50 km (below the centerline) (Fig. 9b). Note that the vortex center as defined by the circulation center (with a minimum wind speed) at 3-km height is less southward so that the vortex center appears to jump over the mountain (figure not shown). At 51 h, the cyclonic vortex near the island becomes mostly northerly at the lee

side and over the mountain, which is much stronger than the southerly wind east of the mountain at 5-km height (Fig. 9b). We found that such stronger northerly wind over the mountain can develop to about 7–8-km height (similar to the development of the stronger wind speed in Fig. 8b). The stronger northerly wind over the mountain range in the midtroposphere supports the sudden south turn of the vortex at this time. In the past 12 h (39–51 h) and 24 h (27–51 h), maximum rainfalls of about 250 and 600 mm, respectively, are produced near the southwestern and southern slopes (figure not shown). The simulated vortex track in WL400 is similar to that in Wu et al. (2015), despite the experiments having some differences in model physics and initial vortex intensity. As the length of mountain range L_y increases to 1000 km, the suddenly southward deflection ahead of the mountain is reduced. Further increase of L_y to 2000 km results in a completely southward deflection without the earlier northward deflection as seen in WL400.

e. Track sensitivity to mountain width and length

The above results show complicated track deflection with respect to varying cyclone intensity and size for a specific smaller mountain range (Figs. 5 and 6). For such a short mountain range (e.g., less than 400 km), the vortex tends to slightly move northward prior to landfall but then suddenly turns southward along the east coast and then jumps over the central mountain. It appears that the smaller vortex generally tends to rebound northward prior to landfall at this specific mountain. Previous studies (Lin et al. 2005; Huang and Lin 2008) have hypothesized an important nondimensional parameter (R_{mw}/L_y) in the determination of the upstream track deflection. Both the above studies did not contain boundary layer turbulent mixing and cloud effects. In this study, we revisit the track sensitivity to this parameter for the cyclone with both physical effects included. For these sensitivity experiments on track, we use one single domain at 15-km resolution, choose a fixed $L_x = 100$ km but vary both L_y (from L1 = 1000 km to L6 = 3500 km) and mountain height h (from H1 = 1500 m to H5 = 3500 m) for a specific vortex with $V_{max} = 20$ m s⁻¹ and $R_{mw} = 80$ km.

Figure 10 shows the simulated tracks under the easterly steering flow of 4 m s⁻¹ from the experiments (with different mountain ranges) in Table 3. The vortex retains a similar initial intensity and keeps a straight westward movement when it is not close to the mountain. For this specific vortex, an increase in mountain height tends to result in increased southward deflection. The southward deflection also becomes more significant as L_y becomes larger (e.g., the rightmost panels). It is

interesting to observe that the early southward deflection, regardless of the lateral extent, is followed by a northward rebound, which appears to be general for all the experiments in Table 3, except when L_y is small. For L_y smaller than 1000 km, the vortex turns slightly northward without an earlier southward deflection as shown and discussed before. We note that the leftmost panels with L1 (1000 km) exhibit qualitatively similar track deflection to that in Fig. 2a of Lin and Savage (2011), where the narrower mountain is used. Some of the vortices seem to drift away from the centerline, as a result of strong deformation of the vortices after passing over a higher and longer mountain range. The translating vortices may not be constrained closely to the initial direction of motion. This does not result from the beta drift since the flow is on an f plane.

It is convenient to highlight the sensitivity of track deflection to the mountain width L_x for an ideal mountain range. For this purpose, a series of experiments with fixed $L_y = 2000$ km and $h = 2000$ m but different L_x were conducted for the same vortex (with $V_{max} = 20$ m s⁻¹ and $R_{mw} = 80$ km) under the easterly steering flow of 4 m s⁻¹. As shown in Fig. 11, the vortex deflects slightly southward prior to landfall, and the deflection is not sensitive to the width (from W1 = 100 km to W6 = 600 km). As the mountain width increases, the northward extent of the rebound after passing over the mountain, however, also increases. On the other hand, the southward deflection is not greatly changed as the vortex intensity increases (figure not shown). The simulation results indicate that the mountain slope (i.e., steepness) may not be a major factor in the determination of upstream track deflection. The track deflection is not sensitive to the width of the mountain range but to its length, which is also shown in the ideal experiments with an intense cyclone in Wu et al. (2015).

f. The mechanism of upstream track deflection with a northward rebound

The channeling effects may play a preceding role in localizing the northerly asymmetric flow near the northeast coast of the mountain for a moderate vortex past a shorter mountain range. For a longer mountain range, the channeling effects may also be responsible for the early southward deflection as the vortex is close to the mountain but cannot explain why the southward deflection is followed by an ensuing northward rebound as shown in some tracks in Fig. 10. The mechanism for the vortex rebounding needs to be explored, and we have chosen W1L3H3 for illustration. As shown in Fig. 12, the vortex translation is straight westward with a similar flow structure before closing to the mountain—for example, by 36 h. At the earlier stage without a track

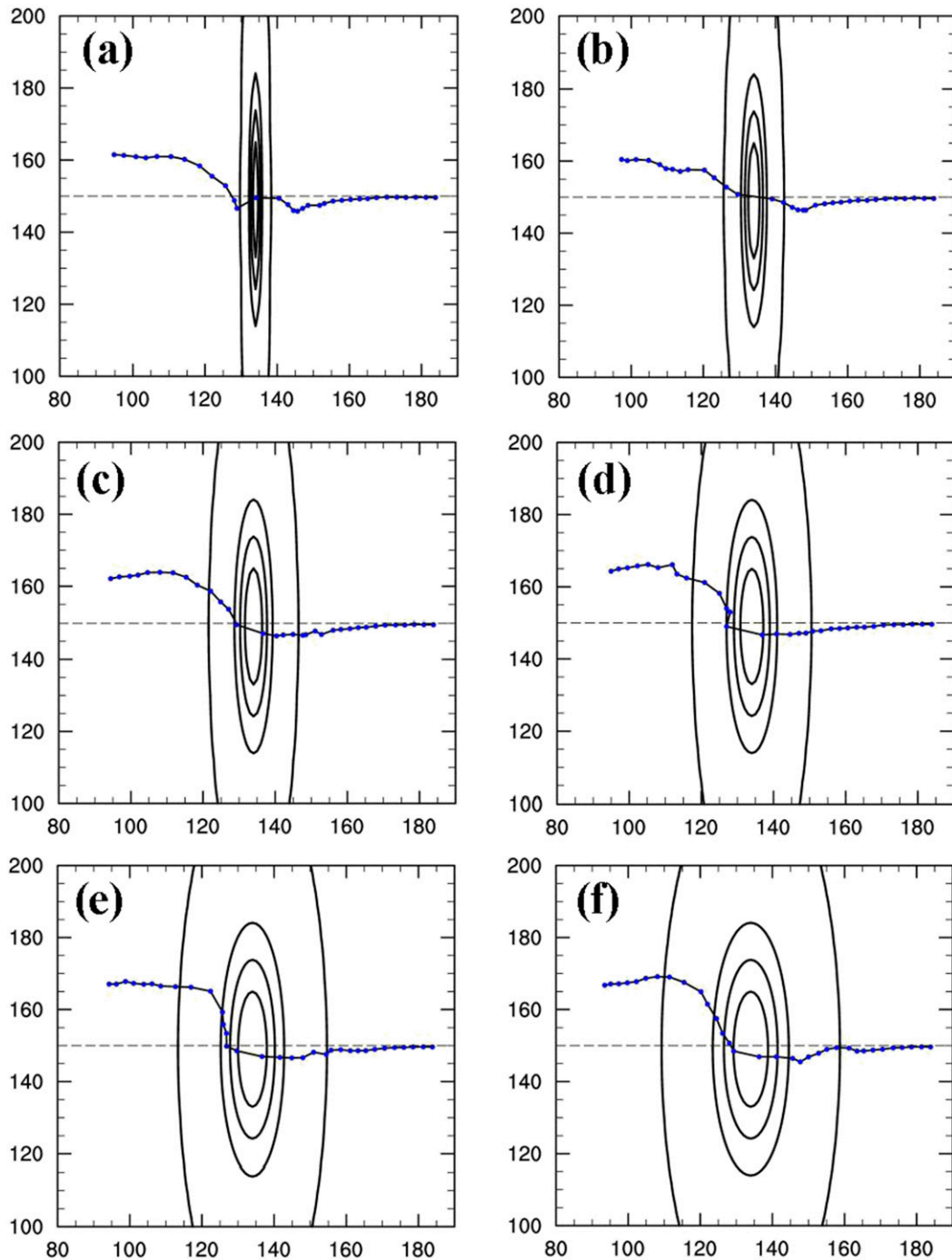


FIG. 11. As in Fig. 10, but with the varying widths for L_x (from $W1 = 100$ km to $W6 = 600$ km). A mountain length L_y of 2000 km and a mountain peak of 2 km are used. The contours represent the terrain height at 1 m, 0.5 km, 1 km, and 1.5 km, respectively. (a) $W1 = 100$ km, (b) $W2 = 200$ km, (c) $W3 = 300$ km, (d) $W4 = 400$ km, (e) $W5 = 500$ km, and (f) $W6 = 600$ km.

deflection, the vortex maintains the stronger wind to the north of the vortex center. The vortex is about to deflect southward when the stronger wind rotates to the west and southwest quadrants of the vortex at 30 h. The

southward deflection increases as the faster-wind zone (i.e., a speedy core) rotates counterclockwise, and it can reach to a maximum as this speedy core resides between the upstream slope of the mountain and the western

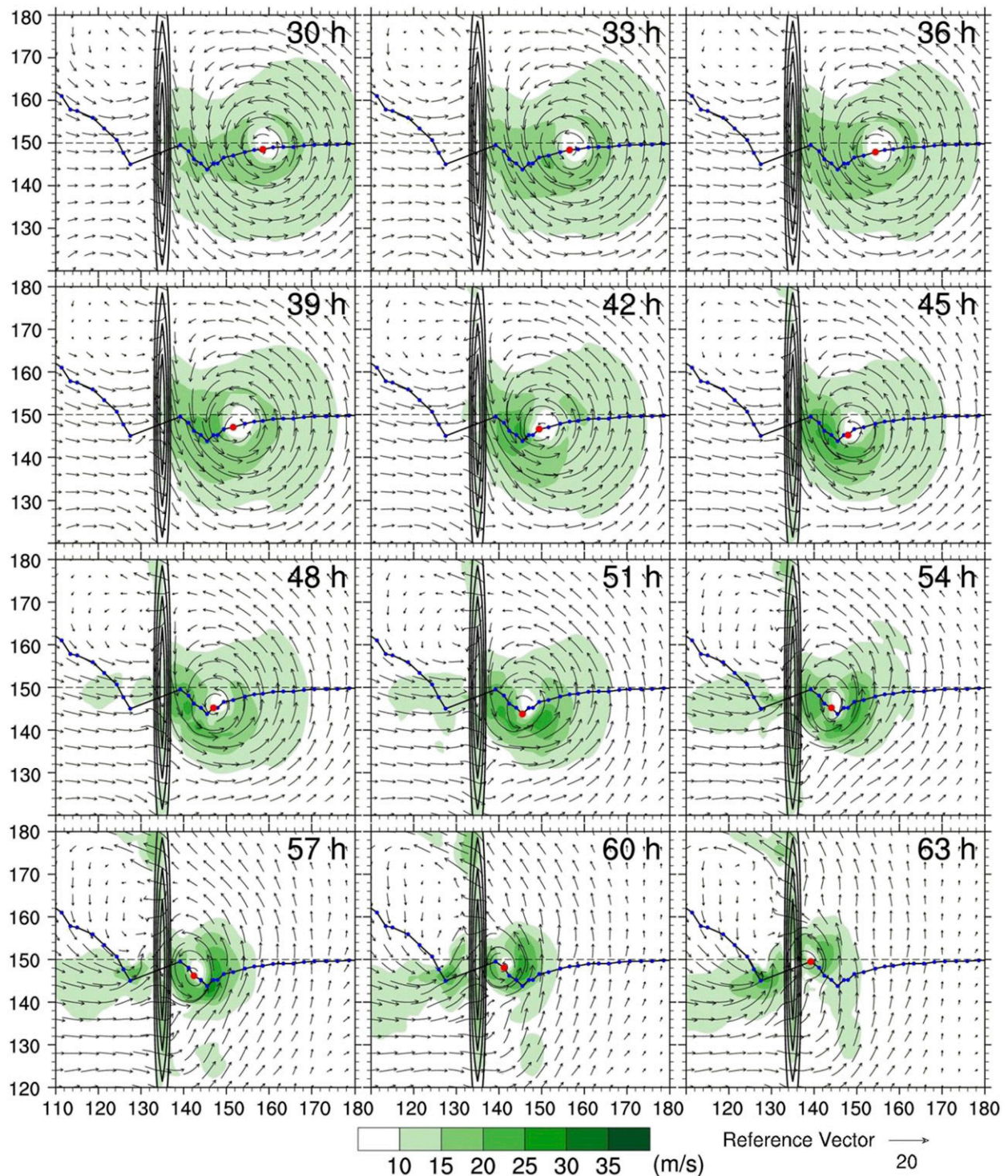


FIG. 12. The evolution of vortex track every 3 h for W1L3H3 overlapped with the wind field averaged by the lowest 11 model levels (about 2-km depth) and subtracting the steering wind speed. Shading represents the horizontal wind speed at an interval of 5 m s^{-1} . The contours represent the terrain heights at 0.5, 1, 1.5, and 2 km, respectively.

flank of the vortex, where a northerly jet is produced as a result of the effects of channeling flow. For a shorter mountain range, the channeling effects are weaker and more localized near the central barrier, thus limiting the extent of the northerly jet for driving the vortex southward as seen in the experiments of L1 series in Table 1. The presence of the northerly jet in the vortex closing to landfall has been a typical inference for the southward deflection of some westward translational cyclones, like Typhoon Krosa (2007) (e.g., Huang et al. 2011; Wu et al. 2015) and the looping track of Typhoon Haitang (2005) (Jian and Wu 2008). The developed height of the speedy core gradually increases as the vortex is approaching the mountain and is slightly above the mountain height when the vortex is near the mountain (figures not shown). As the outer cyclonic vortex flow passes over the southern mountain and interacts with the inner vortex, the speedy core then may advect to the southeast quadrant of the vortex. We found that this process is generally true for all the cases in this study that the vortex will rebound northward when the speedy core rotates counterclockwise into the southeast quadrant of the vortex (e.g., after 51 h). The northward rebound of the vortex may be more limited or even disappear in the presence of a higher and longer mountain range as seen in Fig. 10.

We calculated the vorticity tendency budgets associated with different physical processes for this case (W1L3H3), which were directly computed in the terrain-following coordinates to reduce the interpolation errors (for the vorticity equation, see appendix). As shown in Fig. 13, the vorticity budgets near the surface at 45 h indicate that the southward deflection is mainly in response to vortex stretching just near the speedy core, where significant convergence is produced at low levels with cloud convection (figures not shown). Over the region of positive vorticity stretching, vorticity advection is negative, indicating that larger cyclonic vorticity is exported. The southward deflection reaches a maximum at 51 h as the vortex stretching shifts southeastward (figures not shown). Afterward, the vortex tends to rebound northward coincidentally at the time when the speedy core moves to the eastern flank of the vortex. From 51 h, positive vorticity advection is the dominant term over the central mountain slope, while the vorticity stretching becomes negative there. Other effects (tilting and diffusion) appear secondary (not shown). (Figures 13d and 13f show the budget results at 57 h when the vortex rebounds northward. Vorticity stretching, however, is still positive, and the flow is spiraling with the convective cloud into the vortex core. To the northwest of the vortex center, positive vorticity advection appears overwhelming, owing to the intense swirling flow past the mountain.) These

results tend to support other studies that southward (northward) deflection may be associated with dominant vorticity stretching (vorticity advection) (e.g., Lin et al. 2005; Huang and Lin 2008), despite that this study has included more physics (surface friction, boundary layer turbulent mixing, cloud effects, etc.).

g. The impacts of boundary layer turbulent mixing and cloud effects

Both boundary layer (BL) turbulent mixing and cloud effects (cumulus parameterization and explicit cloud microphysics) may change the vortex structure as well as intensity and thus play a role in the upstream track deflection. The impacts of both effects are explored by two sets of sensitivity experiments. Note that in this study, the surface fluxes are also deactivated in the experiments without BL turbulent mixing. The first set of experiments is similar to WL400 but without BL turbulent mixing (denoted by WL400-B) and without cloud effects (denoted by WL400-M). The second set of experiments is similar to W1L3H3 with $V = 50 \text{ m s}^{-1}$ but without BL turbulent mixing (denoted by W1L3H3-V50-B) and without cloud effects (denoted by W1L3H3-V50-M). The first set of experiments (with the fine domain at 5-km resolution) is intended for comparison on channeling effects with both physics without either of both physics, and the second set of experiments (at 15-km resolution) may reveal how the track deflection of the stronger vortex will be modified when approaching a longer mountain range.

Figure 14 shows the vortex circulation at 1-km height at the fine domain and the associated vertically integrated cloud water for WL400 and WL400-B. At this time (51 h) when the vortex just makes landfall, most of the clouds for WL400 are produced at the northeastern island and the western slope of the mountain. Deactivation of either of the physical processes leads to similar upstream tracks but somewhat less northward than that with the complete physics as the vortex is closer to the mountain. We found that both vortices of WL400-B and WL400-M are straight westward by about 36 h and begin to deflect northward as the outer vortex flow passes around the southern mountain range to converge with the inner vortex flow southeast of the vortex center. For both cases, the convergence produces little rainfall southeast of the vortex center in association with the less-enhanced southerly wind compared to that of WL400 with intense rainfall. Interestingly, both former tracks do not display a rapid south turn as the vortex is close to the mountain base, compared to the latter track with both physics. Without BL turbulent mixing, the vortex produces little clouds over the island in association with the weaker northerly flow along the

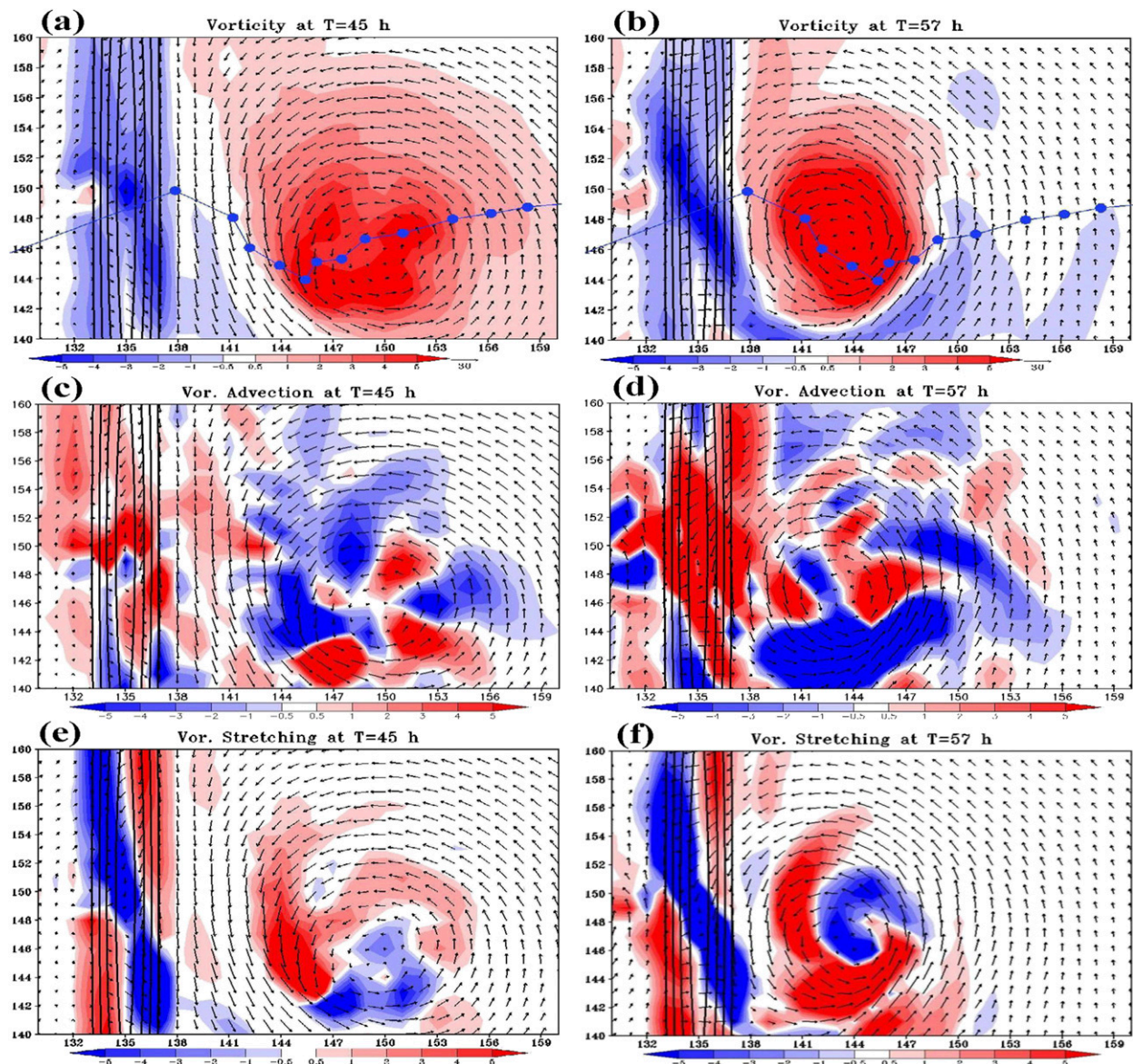


FIG. 13. (a) Vorticity ($\times 10^4 \text{ s}^{-1}$) at the third model level $\sigma = 0.9375$ for W1L3H3 at 45 h. (b) As in (a), but at 57 h. (c) As in (a), but for vorticity advection ($\times 10^8 \text{ s}^{-2}$) at 45 h. (d) As in (c), but at 57 h. (e),(f) As in (c) and (d), respectively, but for vorticity stretching ($\times 10^8 \text{ s}^{-2}$). The contours represent the mountain heights at 0.5, 1, 1.5, and 2 km, respectively. The blue line with dots in (a) and (b) is the vortex track every 3 h determined from the minimum surface pressure perturbation.

mountain (Fig. 14b). Because of the weaker channeling effects, the vortex only undergoes a slightly southward deflection prior to landfall for WL400-B. With the weakest intensity of the vortex when the cloud effects have been deactivated, the southward deflection is further reduced for WL400-M. These experiments show that both physics can modulate the southward deflection of the vortex past a short mountain range as induced by the channeling effects.

Figure 15 shows the vortex circulation at 1-km height and the associated vertically integrated cloud water for

the second set of experiments (W1L3H3-V50, W1L3H3-V50-B, and W1L3H3-V50-M) with a long mountain range. In this set of experiments, the mountain peak is 2.5 km (H3). An additional set of experiments is also conducted with the mountain peak increased to 3.5 km (H5) for comparison. For W1L3H3-V50 (with both physics), the 24-h maximum rainfall in the vortex is about 300–400 mm when the vortex is not close to the mountain. The stronger wind in the vortex with BL turbulent mixing is more localized at 30 h than that without this effect (Fig. 15a vs Fig. 15c). Without BL

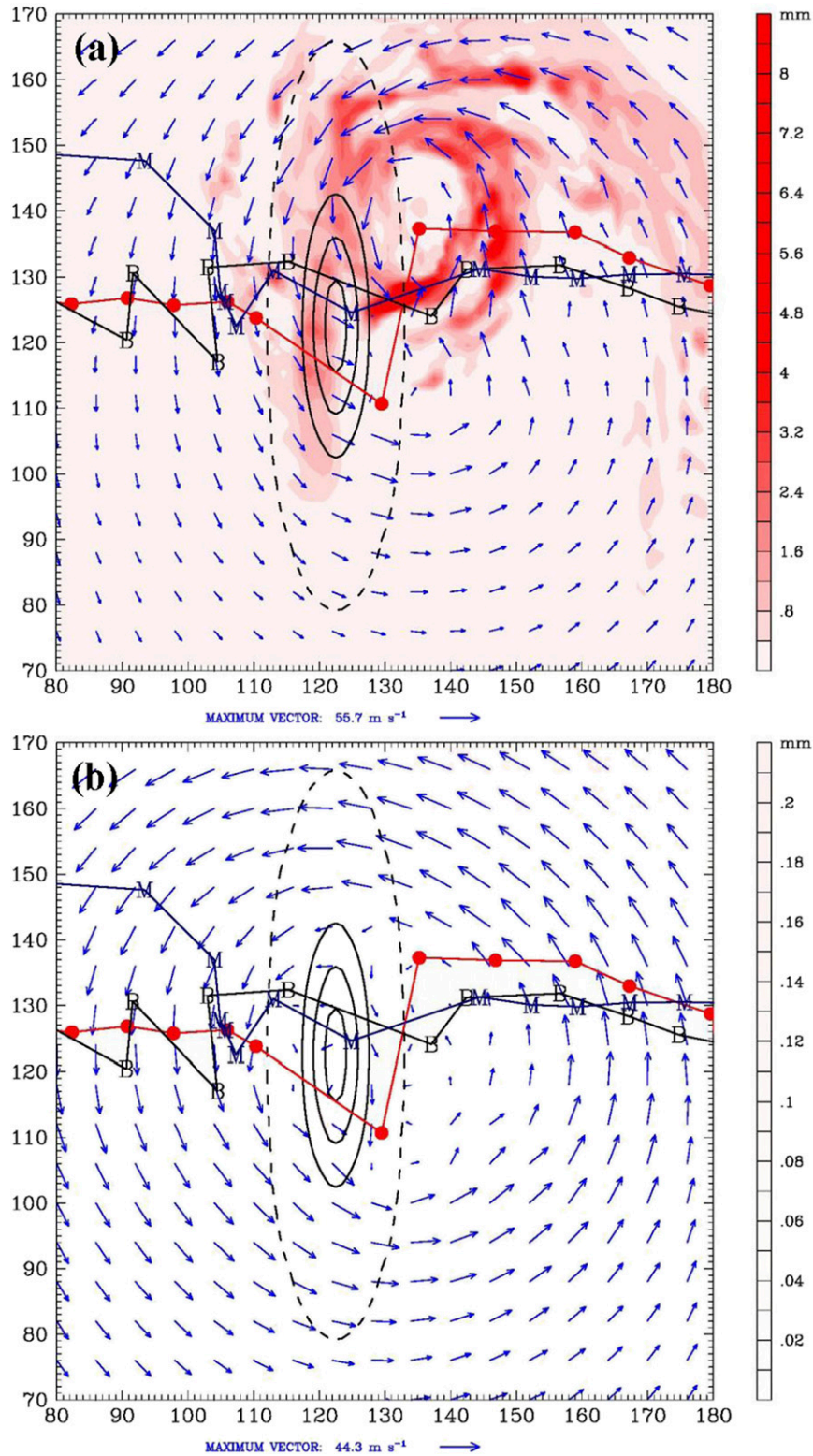


FIG. 14. (a) Horizontal wind (m s^{-1}) at 1-km height and vertically integrated cloud water (shaded, mm) at 51 h at the fine domain for WL400. (b) As in (a), but for WL400-B (without boundary layer turbulent mixing). The red line with dots and the black line marked with “B” represent the vortex tracks near the surface every 3 h for WL400 and WL400-B, respectively. The dark blue line (marked with “M”) is the vortex track every 3 h for WL400-M (without cloud effects). The contours represent the terrain heights as in Fig. 7. The grid interval is 5 km.

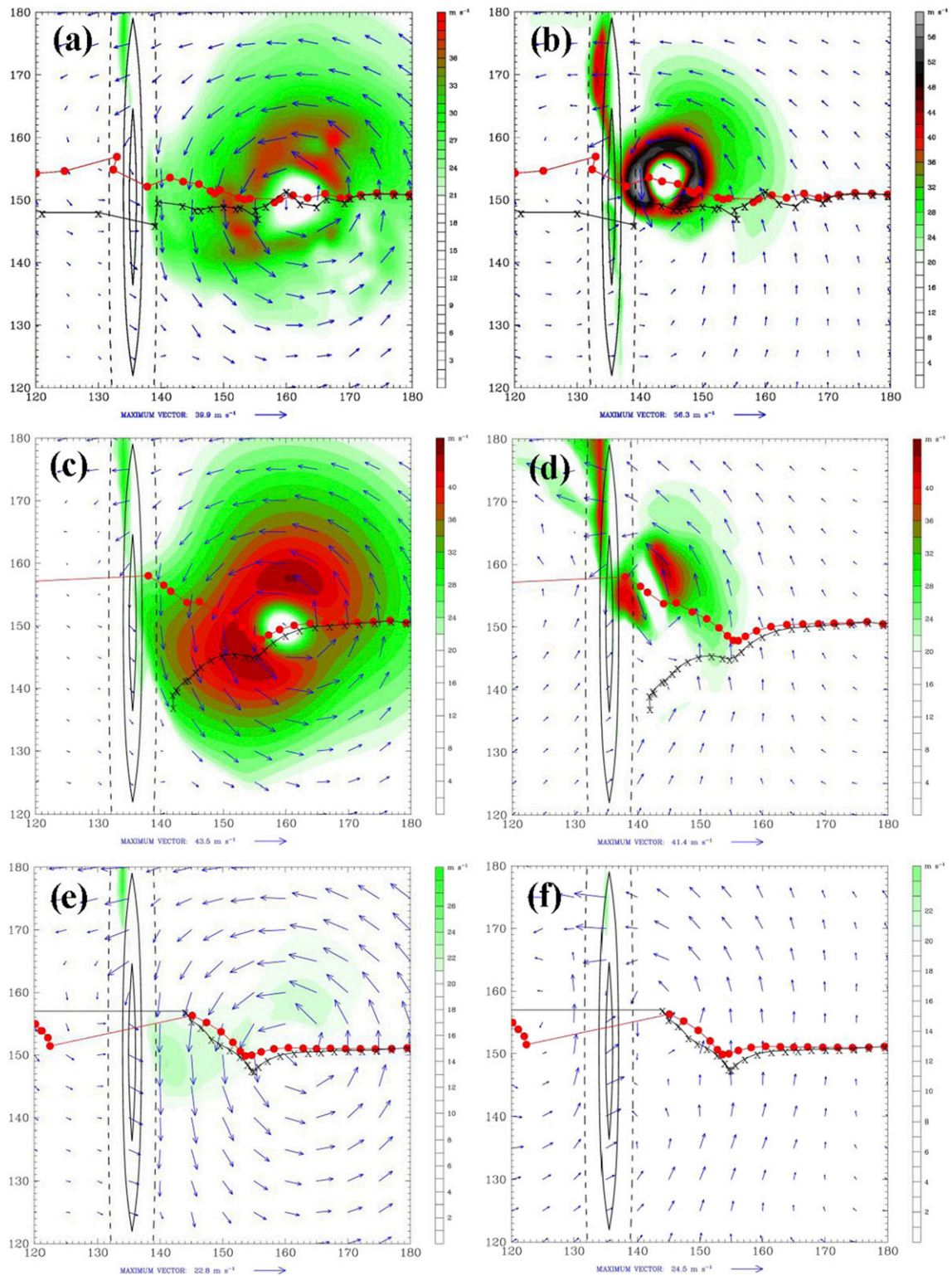


FIG. 15. (a) Horizontal wind at 1-km height and wind speed (shaded, m s^{-1}) at 30 h for W1L3H3-V50. (b) As in (a), but at 60 h. (c),(d) As in (a) and (b), respectively, but for W1L3H3-V50-B (without boundary layer turbulent mixing). (e),(f) As in (a) and (b), respectively, but for W1L3H3-V50-M (without cloud effects). Solid contours are for 1- and 2-km terrain heights and dash contours are for 10-m height. Red lines with dots represent the vortex track near the surface every 3 h for the mountain peak H3 (2.5 km) and black lines marked with \times are for H5 (3.5 km). The grid interval is 15 km.

turbulent mixing, the vortex produces little rainfall (not shown) but is slightly stronger (43.5 m s^{-1}) at this height at this earlier stage compared to that with BL turbulent mixing (39.9 m s^{-1}). Both vortex cores have significantly shrunk as closer to the mountain, but only the vortex with BL turbulent mixing gets intensified (e.g., to 56.3 m s^{-1} at 60 h). The vortex without BL turbulent mixing deflects slightly southward and then rebounds northward as in the weaker-vortex experiment W1L3H3 (see Fig. 12). Without the strong latent heating, the vortex track is similar to that without BL turbulent mixing, despite that the former vortex at low levels is much weaker (e.g., only reaching $22\text{--}25 \text{ m s}^{-1}$ at 1-km height). For both the experiments, the vortex at much higher levels (e.g., 5-km height) passes over the mountain as steered by the easterly environmental flow, while the outer vortex passes over the lower mountain corner and reforms a circulation center farther downwind of the mountain. Thus, both the vortex tracks near the surface appear to jump over the mountain at a speed faster than the upper vortex.

As the mountain peak increases to 3.5 km (H5), the vortex with both physics begins to deflect slightly southward near 30 h and then keeps moving roughly westward with time. A slight south turn of the vortex is also present as the vortex is close to the mountain base owing to the stronger channeling effects associated with the more consolidated vortex core (Fig. 15d). When BL turbulent mixing is deactivated in this case, most of the outer vortex flow at lower levels cannot pass over such a high mountain and instead remains east of the mountain with a southward track after 60 h (Fig. 15d) without forming a downwind circulation center; the vortex at much higher levels remains westward with time. The inner vortex at lower levels gradually shrinks and then disappears southeast of this higher mountain.

When only latent heating is turned off in W1L3H3-V50-M, the parent vortex at 1-km height still resides east of the mountain after 60 h (Fig. 15f). As can be seen, the vortex slightly deflects southward at the earlier stage but then also rebounds northward and jumps over the mountain. This jumpover is because a new vortex center can reform farther downwind of the mountain as discussed earlier. During the southward track deflection, the speedy zone also extends between the mountain and the western flank of the vortex, consistent with the mechanisms addressed in the previous section for the weaker-vortex case (W1L3H3). We found that the upstream southward track deflection is about the same when both BL turbulent mixing and cloud effects are deactivated in this experiment. When the steering flow is increased to 8 m s^{-1} , the upstream vortex tracks for the above three experiments remain similar with a slightly

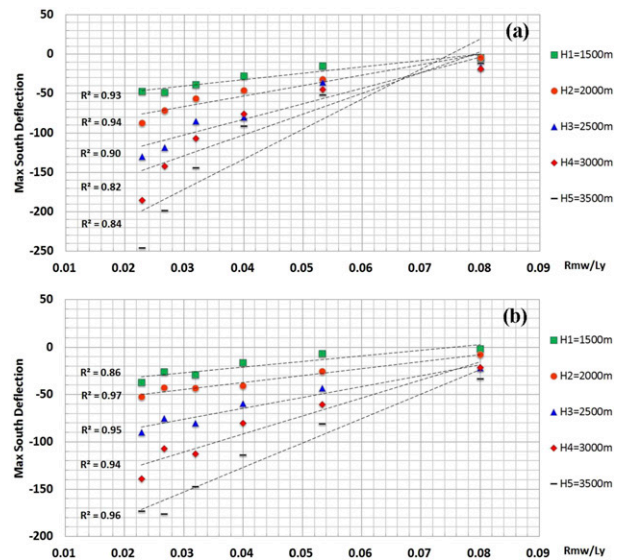


FIG. 16. (a) The linear regression between the maximum upstream southward deflection distance (km) and the nondimensional parameter R_{mw}/L_y for the slower steering wind speed of 4 m s^{-1} . (b) As in (a), but for the faster steering wind speed of 8 m s^{-1} .

less southward deflection and then a northward rebound. However, the vortex core without BL physics completely vanishes near the mountain range when the mountain is higher ($H5 = 3.5 \text{ km}$) and the outer vortex flow cannot form a new center downwind of the mountain. Compared to the effects of latent heating, BL turbulent mixing appears to have a larger influential role in the track deflection near the mountain.

h. The controlling parameter for track deflection

One objective of this paper is to establish a clear relationship that connects the track deflection to some potential parameters as previously discussed in Lin et al. (2005) and Huang and Lin (2008). The track deflection is generally viewed as a consequence of terrain blocking that intercepts the cyclonic vortex, more or less, depending on the lateral extension of the terrain perpendicular to the direction of the vortex translation. Thus, the extent of terrain blocking can be measured by the ratio of the vortex size and terrain length, or likely their proxy R_{mw}/L_y . Herein, R_{mw} uses the initial value of the vortex as an effective representative of the vortex size since the vortex keeps similar intensity and structure before closing to the mountain (see Fig. 12). The linear regressions for both steering wind speeds of 4 and 8 m s^{-1} between the upstream deflection and the nondimensional parameter R_{mw}/L_y are given in Fig. 16. As seen for both steering winds, the R^2 coefficients are rather high—all above 0.8 and some over 0.9. The southward deflection increases with decreasing R_{mw}/L_y ,

which is enhanced about linearly with mountain height for a given ratio of R_{mw}/L_y , except for the slower vortex past a long and high mountain ($h = 3500$ m). Thus, the linear regression is not well established for a vortex past a large and high mountain range, denoting that nonlinearity in the regression is possible. Nevertheless, such L_y over 3000 km is hypothetical for investigation.

Figure 16 also indicates a reduction in the vortex track deflection as the steering-flow intensity increases, which has been shown in other studies but without giving such a relationship (e.g., Yeh and Elsberry 1993a; Lin et al. 2005; Huang and Lin 2008; Wu et al. 2015). From the systematic experiments, there is about 50% reduction in the maximum deflection distance as the steering-flow speed is doubled (Fig. 16b). Less track deflection results partially from a shorter passage time for a faster translational vortex past the mountain barrier. Again, the extent of southward deflection also increases with increased mountain height, in consistency with stronger terrain blocking.

4. Conclusions

In this paper, we aim to clarify the upstream track deflection of a propagating cyclonic vortex past a mountain range by utilizing the WRF Model with ideal initial conditions for both the steering flow and vortex. The model experiments include both boundary layer (BL) turbulent mixing and cloud effects. Our results with more complete physics are consistent with upstream track deflection of the inviscid stratified dry vortex and shallow-water vortex past similar mountain ranges (e.g., Lin et al. 2005; Huang and Lin 2008). This implies that both vortex Froude number (V_{max}/Nh) and steering-flow Froude number (U/Nh) would influence the degree of deflection but essentially have no control on the direction of upstream track deflection. The direction of upstream track deflection is found to be mainly controlled by the nondimensional parameter (R_{mw}/L_y) where R_{mw} is the vortex size (represented by the radius of the maximum wind) and L_y is the north-south length scale of the mountain for a westbound vortex. The results from a series of control experiments for the frictional, moist vortex reveal that linear regression for given steering flow and mountain height can be clearly established between the maximum upstream deflection distance and the nondimensional parameter R_{mw}/L_y , with the R^2 coefficients reaching around 0.9 or higher. For a westbound vortex approaching a higher and longer mountain range, upstream southward deflection may be induced. The southward deflection distance increases with smaller R_{mw}/L_y , and higher mountains for both weaker and stronger steering flow. When the

steering-flow intensity is doubled, the southward deflection of the vortex is roughly reduced by 50%.

The southward deflection of a westbound vortex near the mountain base is primarily controlled by the convergence (stretching) effect due to the combination of the speedy core at the southwestern flank of the vortex and a northerly jet between the vortex and the mountain stemming from the effects of channeling flow. The vortex then starts to rebound northward to pass over the mountain as the speedy core rotates counterclockwise to the eastern flank of the vortex, regardless of the degree of southward deflection. Deactivation of BL turbulent mixing and/or cloud effects may reduce the southward track deflection due to the weaker channeling effects. In the absence of BL turbulent mixing, the vortex at low levels deflects southward and is blocked upstream of the high mountain, whether or not cloud effects are activated.

In this study, we also examine the influence of the channeling effect on vortex track deflection. In our simulation for a shorter mountain range, the northward deflected vortex takes a sudden south turn when it is close to the mountain base. The sudden south turn of the vortex can be attributed to the generalized effects of the channeling flow at upper levels that induce the stronger northerly wind over the mountain range rather than east of the mountain to drive the vortex southward as shown in Wu et al. (2015). In contrast to Wu et al., however, when the mountain range is much longer (e.g., 2000 km long), the channeling effects are essentially stronger at lower levels but are more localized near the mountain base and will not lead to such a sudden south turn of the vortex without the induced stronger northerly wind over the mountain range. On the other hand, in the presence of a shorter mountain range, the outer cyclonic vortex at low levels can pass over and around the northern mountain range and thus the vortex does not turn south.

In this study, we have not explicitly included the role of V_{max} in upstream track deflection. The track deflection for an inviscid vortex has been connected with the vortex Froude number (V_{max}/Nh) (Lin et al. 2005; Huang and Lin 2008). In general, a stronger vortex with a larger Froude number tends to deflect rightward as more cyclonic flow can be less blocked as to pass around or over the mountain barrier. The vortex may get stronger through development of convective intensification (Nolan et al. 2007) or favorable underlying conditions (e.g., Emanuel 1988). It is thus less attributable to a fixed intensity in the regression for a developing cyclone. In addition, an intense tropical cyclone may also undergo a curved track when strong asymmetric convection is being produced in the eyewall

and the outer vortex, leading to an uncertainty in metrics of the track deflection. Nevertheless, track deflection of a quasi-steady intense typhoonlike vortex past a mountain in various steering environments is another challenging issue to be tackled in a future study.

Acknowledgments. This study was supported by Ministry of Science and Technology (MOST) in Taiwan under Grant MOST 104-2111-M-008-019.

APPENDIX

The Equation of Vorticity Budgets in the Terrain-Following Coordinate

The equation of absolute vorticity ($\zeta + f$) in the height coordinate is given by

$$\begin{aligned} \frac{\partial}{\partial t}(\zeta + f) = & -\mathbf{U} \cdot \nabla(\zeta + f) - (\zeta + f)(u_x + v_y) \\ & - (w_x v_z - w_y u_z) + \frac{1}{\rho^2}(\rho_x p_y - \rho_y p_x) \\ & + (F_{vx} - F_{uy}), \end{aligned} \tag{A1}$$

where ζ is relative vorticity, f is the planetary vorticity, \mathbf{U} is the wind vector (u, v, w), ρ is the density, p is pressure, and F_u and F_v are turbulent mixing in the u - and v -momentum equations, respectively. The term on the left side of (A1) represents the local time change rate of absolute vorticity, and the terms on the right side represent contributions from advection, stretching, tilting, solenoidal effects, and turbulent mixing, respectively. For the definition of the terrain-following coordinate σ in WRF,

$$\sigma(x, y, z) = \frac{p_h(x, y, z) - p_t}{p_{hs}(x, y) - p_t} = \frac{p_h(x, y, z) - p_t}{\mu}, \tag{A2}$$

where the model dry pressure $\mu = p_{hs} - p_t$, p_h is the hydrostatic pressure, p_{hs} is the surface hydrostatic pressure along the terrain, and p_t is the pressure at the model top. All the terms in (A1) can be transformed to the σ coordinate:

$$-\mathbf{U} \cdot \nabla(\zeta + f) = -u \frac{\partial(\zeta + f)}{\partial x} - v \frac{\partial(\zeta + f)}{\partial y} - \dot{\sigma} \frac{\partial(\zeta + f)}{\partial \sigma}, \tag{A3}$$

$$-(\zeta + f)(u_x + v_y) = -(\zeta + f)(u_x + u_\sigma \sigma_x + v_y + v_\sigma \sigma_y), \tag{A4}$$

$$\begin{aligned} -(w_x v_z - w_y u_z) = & -[(w_x + w_\sigma \sigma_x) v_\sigma \sigma_z \\ & - (w_y + w_\sigma \sigma_y) u_\sigma \sigma_z], \end{aligned} \tag{A5}$$

$$\begin{aligned} \frac{1}{\rho^2}(\rho_x p_y - \rho_y p_x) = & \frac{1}{\rho^2}[(\rho_x + \rho_\sigma \sigma_x)(p_y + p_\sigma \sigma_y) \\ & - (\rho_y + \rho_\sigma \sigma_y)(p_x + p_\sigma \sigma_x)], \end{aligned} \tag{A6}$$

and

$$F_{vx} - F_{uy} = (F_{vx} + F_{v\sigma} \sigma_x) - (F_{uy} + F_{u\sigma} \sigma_y), \tag{A7}$$

where $\zeta = v_x - u_y$ is computed in σ coordinate as $v_x \sigma_x - u_y \sigma_y$, $\dot{\sigma} = D\sigma/Dt$ denotes the equivalent vertical velocity in the σ coordinate, and the above coordinate derivatives are given by

$$\sigma_x = \frac{p_{hx}}{\mu} - \frac{\mu_x}{\mu} \sigma, \tag{A8}$$

$$\sigma_y = \frac{p_{hy}}{\mu} - \frac{\mu_y}{\mu} \sigma, \text{ and} \tag{A9}$$

$$\sigma_z = \frac{p_{hz}}{\mu}. \tag{A10}$$

Calculation of the vorticity budgets in σ coordinates can avoid the interpolation errors since the model variables as well as F_u and F_v are given in σ coordinates.

REFERENCES

Bender, M. A., R. E. Tuleya, and Y. Kurihara, 1987: A numerical study of the effect of island terrain on tropical cyclones. *Mon. Wea. Rev.*, **115**, 130–155, doi:10.1175/1520-0493(1987)115<0130:ANSOTE>2.0.CO;2.

Brand, S., and J. W. Blelloch, 1974: Changes in the characteristics of typhoons crossing the island of Taiwan. *Mon. Wea. Rev.*, **102**, 708–713, doi:10.1175/1520-0493(1974)102<0708:CITCOT>2.0.CO;2.

Chan, C. L., and R. T. Williams, 1987: Analytical and numerical studies of the beta-effect in tropical cyclone motion. Part I: Zero mean flow. *J. Atmos. Sci.*, **44**, 1257–1265, doi:10.1175/1520-0469(1987)044<1257:AANSOT>2.0.CO;2.

Chang, S. W.-J., 1982: The orographic effects induced by an island mountain range on propagating tropical cyclones. *Mon. Wea. Rev.*, **110**, 1255–1270, doi:10.1175/1520-0493(1982)110<1255:TOEIBA>2.0.CO;2.

Emanuel, K. A., 1988: Toward a general theory of hurricanes. *Amer. Sci.*, **76**, 370–379.

Hong, S.-Y., and J.-O. J. Lim, 2006: The WRF single-moment 6-class microphysics scheme (WSM6). *J. Korean Meteor. Soc.*, **42**, 129–151.

—, Y. Noh, and J. Dudhia, 2006: A new vertical diffusion package with an explicit treatment of entrainment processes. *Mon. Wea. Rev.*, **134**, 2318–2341, doi:10.1175/MWR3199.1.

Hsu, L.-H., H.-C. Kuo, and R. G. Fovell, 2013: On the geographic asymmetry of typhoon translation speed across the mountainous island of Taiwan. *J. Atmos. Sci.*, **70**, 1006–1022, doi:10.1175/JAS-D-12-0173.1.

Huang, C.-Y., and Y.-L. Lin, 2008: The influence of meso-scale mountains on vortex tracks: Shallow-water modeling study. *Meteor. Atmos. Phys.*, **101**, 1–20, doi:10.1007/s00703-007-0284-1.

Huang, Y.-H., C.-C. Wu, and Y. Wang, 2011: The influence of island topography on typhoon track deflection. *Mon. Wea. Rev.*, **139**, 1708–1727, doi:10.1175/2011MWR3560.1.

- Jian, G.-J., and C.-C. Wu, 2008: A numerical study of the track deflection of Supertyphoon Haitang (2005) prior to its landfall in Taiwan. *Mon. Wea. Rev.*, **136**, 598–615, doi:10.1175/2007MWR2134.1.
- Jordan, C. L., 1958: Mean soundings for the West Indies area. *J. Atmos. Sci.*, **15**, 91–97, doi:10.1175/1520-0469(1958)015<0091:MSFTWI>2.0.CO;2.
- Kuo, H.-C., R. T. Williams, J.-H. Chen, and Y.-L. Chen, 2001: Topographic effects on barotropic vortex motion: No mean flow. *J. Atmos. Sci.*, **58**, 1310–1327, doi:10.1175/1520-0469(2001)058<1310:TEOBVM>2.0.CO;2.
- Lin, Y.-L., and L. C. Savage, 2011: Effects of landfall location and the approach angle of a cyclone vortex encountering a mesoscale mountain range. *J. Atmos. Sci.*, **68**, 2095–2106, doi:10.1175/2011JAS3720.1.
- , J. Han, D. W. Hamilton, and C.-Y. Huang, 1999: Orographic influence on a drifting cyclone. *J. Atmos. Sci.*, **56**, 534–562, doi:10.1175/1520-0469(1999)056<0534:OIOADC>2.0.CO;2.
- , S.-Y. Chen, C. M. Hill, and C.-Y. Huang, 2005: Control parameters for the influence of a mesoscale mountain range on cyclone track continuity and deflection. *J. Atmos. Sci.*, **62**, 1849–1866, doi:10.1175/JAS3439.1.
- Nolan, D. S., 2011: Evaluating environmental favorableness for tropical cyclone development with the method of point-downscaling. *J. Adv. Model. Earth Syst.*, **3**, M08001, doi:10.1029/2011MS000063.
- , Y. Moon, and D. P. Stern, 2007: Tropical cyclone intensification from asymmetric convection: Energetics and efficiency. *J. Atmos. Sci.*, **64**, 3377–3405, doi:10.1175/JAS3988.1.
- Skamarock, W. C., and Coauthors, 2008: A description of the Advanced Research WRF version 3. NCAR Tech. Note NCAR/TN-475+STR, 113 pp., doi:10.5065/D68S4MVH.
- Smith, R. B., 1993: A hurricane beta-drift law. *J. Atmos. Sci.*, **50**, 3213–3215, doi:10.1175/1520-0469(1993)050<3213:AHBDL>2.0.CO;2.
- Stern, D. P., and D. S. Nolan, 2011: On the vertical decay rate of the maximum tangential winds in tropical cyclones. *J. Atmos. Sci.*, **68**, 2073–2094, doi:10.1175/2011JAS3682.1.
- Tiedtke, M., 1989: A comprehensive mass flux scheme for cumulus parameterization in large-scale models. *Mon. Wea. Rev.*, **117**, 1779–1800, doi:10.1175/1520-0493(1989)117<1779:ACMFSF>2.0.CO;2.
- Wang, S.-T., 1980: Prediction of the movement and strength of typhoons in Taiwan and its vicinity. National Science Council Research Rep. 108, 100 pp.
- Wu, C.-C., T.-H. Li, and Y.-H. Huang, 2015: Influence of mesoscale topography on tropical cyclone tracks: Further examination of the channeling effect. *J. Atmos. Sci.*, **72**, 3032–3050, doi:10.1175/JAS-D-14-0168.1.
- Yeh, T.-C., and R. L. Elsberry, 1993a: Interaction of typhoons with the Taiwan topography. Part I: Upstream track deflections. *Mon. Wea. Rev.*, **121**, 3193–3212, doi:10.1175/1520-0493(1993)121<3193:IOTWTT>2.0.CO;2.
- , and —, 1993b: Interaction of typhoons with the Taiwan topography. Part II: Continuous and discontinuous tracks across the island. *Mon. Wea. Rev.*, **121**, 3213–3233, doi:10.1175/1520-0493(1993)121<3213:IOTWTT>2.0.CO;2.
- Zehnder, J. A., 1993: The influence of large-scale topography on barotropic vortex motion. *J. Atmos. Sci.*, **50**, 2519–2532, doi:10.1175/1520-0469(1993)050<2519:TIOLST>2.0.CO;2.
- , and M. J. Reeder, 1997: A numerical study of barotropic vortex motion near a large-scale mountain range with application to the motion of tropical cyclones approaching the Sierra Madre. *Meteor. Atmos. Phys.*, **64**, 1–19, doi:10.1007/BF01044127.